Consistent lattice Boltzmann modeling of low-speed isothermal flows at finite Knudsen numbers in slip-flow regime. II. Application to curved boundaries

Goncalo Silva*

LAETA, IDMEC, Mechanical Engineering Department, Instituto Superior Tecnico, Universidade de Lisboa, Av. Rovisco Pais 1, 1049-001, Lisbon, Portugal

(Received 7 June 2018; published 7 August 2018)

Gaseous flows inside microfluidic devices often fall in the slip-flow regime. According to this theoretical description, the Navier-Stokes model remains applicable in bulk, while at solid walls a slip velocity boundary model shall be considered. Physically, it is well established that, to properly account for the wall curvature, the wall slip velocity must be determined by the shear stress, rather than the normal component of the velocity derivative alone, as commonly applied to planar surfaces. It follows that the numerical transcription of this type of boundary condition is generally a challenging task for standard computational fluid dynamics (CFD) techniques. This paper aims to show that the realization of the slip velocity condition on arbitrarily shaped boundaries can be accomplished in a natural way with the lattice Boltzmann method (LBM). To substantiate this conclusion, this work undertakes the following three studies. First, we examine the conditions under which the generic reflection-type boundary rules used by LBM become consistent models for the slip velocity boundary condition. This effort makes use of the second-order Chapman-Enskog expansion method, where we address both planar and curved boundaries. The analysis also clarifies the capabilities and limitations behind the considered reflection-type slip schemes. Second, we revisit the family of parabolic accurate LBM slip boundary schemes, originally formulated in [Phys. Rev. E **96**, 013311 (2017)] on the basis of the multireflection framework, and discuss their characteristics when operating on curved boundaries as well as the limitations of other less accurate LBM slip boundary formulations, such as the linearly accurate slip schemes and the widely popular "kinetic-based" boundary schemes. In addition, we also discuss the numerical stability of the parabolic slip schemes previously developed, providing an heuristic strategy to improve their stable range of operation. Third, we evaluate the performance of the several slip boundary schemes debated in this paper. The numerical tests correspond to two classical 2D benchmark flow problems of slip over non-planar solid surfaces, namely: (i) the velocity profile of the cylindrical Couette flow, and (ii) the permeability of a slow rarefied gas over a periodic array of circular cylindrical obstacles. The obtained numerical results confirm the competitiveness of the LBM when equipped with slip boundary schemes of parabolic accuracy as CFD tool to simulate slippage phenomena over arbitrarily non-planar surfaces. Indeed, although operating on a simple uniform mesh discretization, the LBM yields a similar, or even superior, level of accuracy compared to state-of-the-art FEM simulations conducted on hardworking body-fitted meshes. This conclusion establishes the LBM as a very appealing CFD technique for simulating microfluidic flows in the slip-flow regime, a result that deserves further exploration in future studies.

DOI: 10.1103/PhysRevE.98.023302

I. INTRODUCTION

In microscale gaseous flows the degree of departure from classical hydrodynamic theory is measured by the Knudsen number: $\mathrm{Kn} = \lambda/H$, with λ the mean-free path of gas molecules and H the characteristic length scale of the flow system [1–4]. Based on Kn, it is commonly accepted the existence of four physical regimes: (i) the hydrodynamic- or continuum-flow regime ($\mathrm{Kn} \leqslant 0.001$), (ii) the slip-flow regime ($0.001 < \mathrm{Kn} \leqslant 0.1$), (iii) the transition-flow regime ($0.1 < \mathrm{Kn} \leqslant 10$), and (iv) the free molecular-flow regime ($\mathrm{Kn} > 10$). This work focuses on the hydrodynamic- and slip-flow regimes, since the interval $\mathrm{Kn} \lesssim 0.1$ covers the generality of microfluidic flow applications [5–9].

It is well established, e.g., Refs. [10,11], that the miniaturization of fluidic processes produces a dramatic increase in the surface-to-volume ratio, which credits surface related phenomena the dominant role. While this characteristic offers many technological advantages, as exploited in microelectromechanical systems (MEMS) [6,7,10], the scale reduction also brings new challenges. A fundamental problem refers to the interaction between the fluid flow constituents and the bounding walls. With the growth of the Kn number, new phenomenological features are expected to emerge due to an insufficient number of gas molecules within the sampling region. According to slip-flow theory, the scarcity of gas molecules is only relevant at the walls' vicinity. This hypothesis, therefore, implies that the Navier-Stokes model remains valid in bulk, whereas at boundaries the standard no-slip condition shall be replaced by a slip one, e.g., Refs. [3,8,12–14]. Here, the concept of slip boundary condition arises as a means to account for the effects of the nonequilibrium Knudsen layer, which forms adjacent to solid walls, but without explicitly resolving it when solving for the velocity field. The idea is that, up to $\mathrm{Kn} \lesssim 0.1$, the Knudsen layer is sufficiently thin so that its

*goncalo.nuno.silva@gmail.com

 ©2018 American Physical Society

TABLE I. Examples of slippage coefficient $\mathcal{C}$ values determined through different approaches; a more complete list can be found in [8,9,12]. The parameter σ_v is the tangential momentum accommodation coefficient (TMAC). For most surfaces $\sigma_v \in [0.6, 1]$ [9], where $\sigma_v = 1$ corresponds to fully diffusive walls. In bulk, the collision models considered are Hard Sphere (HS) and BGK models.

References	$\mathcal{C}$	Collision model	Approach
Wall's Reflection Law: *Specular* ($\sigma_v = 0$) to *Diffuse* ($\sigma_v = 1$)			
Maxwell (1987) [23]	$\frac{2-\sigma_v}{\sigma_v}$	–	Elementary kinetic theory
Gross *et al.* (1957) [24–26]	$\frac{2-\sigma_v}{\sigma_v}[\frac{5}{8}\sqrt{\pi}\frac{3.193+\sigma_v}{3.603+0.524\sigma_v}]$	HS	Four moment approx. to half-ranged moment method
Maurer *et al.* (2003) [27]	$1+6\frac{2-\sigma_v}{\sigma_v}\mathrm{Kn}$	–	Experimental measurements
Struchtrup *et al.* (2008) [28–30]	$\frac{2-\sigma_v}{\sigma_v}[\frac{(13-\sqrt{70\pi})\sigma_v+2\sqrt{70\pi}}{(12-\sqrt{70\pi})\sigma_v+2\sqrt{70\pi}}]$	BGK	R13 moment equations
Wall's Reflection Law: *Diffuse*			
Cercignani (1968) [1,31,32]	[0.962,1.019]	Different models	Numerical quadrature and variational procedure
Willis (1691) [33], Kogan (1696) [3]	1.0122	BGK	Integromoment method
Sone *et al.* (1969) [13,19,20,22]	0.98733 / 1.01619	HS / BGK	Asymptotic theory
Loyalka *et al.* (1975) [2,26,34,35]	1.0161941832335	BGK	Exact numerical calculations

effect may be assumed as compressed to a discontinuous jump in the fluid/wall velocity accommodation [3,13,15]. Such a description has a firm theoretical basis. For instance, it can be systematically derived from an asymptotic analysis of the Boltzmann equation, as explained in the classical textbooks by Sone [13,15] and the complementary publications [16–22] where this topic is discussed in depth.

This work focuses on single component gases under isothermal conditions. Such an assumption guarantees that no mass diffusion and heat flow exist. On this basis, the generic slip boundary condition formulates as the jump between the tangential components of the fluid velocity $\vec{u}$ and the wall velocity $\vec{u}_w$ exclusively controlled by the shear stress τ_{ij} at the wall (where $\vec{n}$ and $\vec{t}$ are the normal and tangent unit vectors at the surface):

$$\left(u_i - u_{w_i}\right) t_i = \mathcal{C}\,\frac{\lambda}{\mu}\tau_{ij}\, n_i\, t_j. \tag{1}$$

Here, we will consider Newtonian fluids, where the stress tensor is given by $\tau_{ij} = \mu(\frac{\partial u_i}{\partial x_j} + \frac{\partial u_j}{\partial x_i})$. The other parameters featuring in the slip model, Eq. (1), are the mean-free path λ, the dynamic viscosity μ, and the slippage coefficient $\mathcal{C}$; the latter may take different values as illustrated in Table I. While higher-order slip models have been developed for arbitrary shaped solid surfaces [13,19,20], their application is usually limited to planar walls. For example, the isothermal second-order slip condition applied to curved walls introduces two extra corrective terms, related to the surface curved, which find no counterpart in the plane wall case, e.g., refer to Eq. (3.61a) in Ref. [13]. So far, the gains attainable by this added complexity have not been explored much. For that reason, in this work, we shall not address the modeling of higher-order slip models on curved surfaces, restricting ourselves to the use of Eq. (1).

From the practical standpoint, the major asset of slip-flow theory is the drastic simplification offered in the modeling of finite Kn flows. Thanks to its self-consistent structure—i.e., the standard no-slip condition, $(u_i - u_{w\,i})\,t_i = 0$, is retrieved in the $\mathrm{Kn} \to 0$ limit—it naturally applies to the framework of ordinary hydrodynamic-type equations, thus extending them to finite Kn applications. Such a feature is particularly attractive for computational fluid dynamics (CFD) studies. In this context, most of literature related to the numerical simulation of the Navier–Stokes equations with slip boundary conditions is based on the finite element method (FEM); see Refs. [36,37]. Yet, in this study we focus on an alternative CFD perspective: the lattice Boltzmann method (LBM). The justification for the LBM choice in the context of slip-flow problems shall be the main topic of this work. To support this choice, the relative accuracy between LBM and FEM will also be examined in this work.

In the recent years the LBM has attracted much attention in the modeling and simulation of a variety of fluid flow problems, examples can be found in Refs. [38–41] and references therein. A key reason for the LBM success lies in the simplicity of its working principle. The stream-and-collide structure of the standard LBM algorithm runs on an uniform Cartesian mesh, thus rendering the meshing of complex geometries straightforward. The flipside is that the information on the wall shape must be incorporated in the LBM boundary rule. Therefore, how accurate complex shapes can be represented within the LBM discretization comes dictated by the accuracy of the LBM boundary condition. This explains the large body of literature published on the topic of LBM boundary conditions, e.g., Refs. [40,42–48].

At the present, the implementation of the *no-slip* condition by LBM boundary schemes is well developed for generic, planar, and curved geometries; this fact is illustrated by the extensive reference list given at the end of the previous paragraph. In a different manner, the treatment of *slip* walls has received considerable less attention. So far, the majority of LBM studies [49–60] that have addressed this topic explored the relationship between the LBM equation and the Boltzmann-BGK equation. By doing so, they have attempted to derive LBM discrete analogues of boundary schemes pertaining to the kinetic theory of gases. Unfortunately, the slip

prescribed by these "kinetic-based" schemes is contaminated by unavoidable discrete lattice effects [61–64]. Aiming at overcoming this deficiency, dedicated studies [55,62,65–67] have proposed an *a priori* calibration of the numerical coefficients of these "kinetic-based" schemes. The idea is to "absorb" into physical terms the numerically generated slip. However, this procedure lacks generality, being limited to straight, lattice-aligned channel-like configurations, where an exact solution of the numerical scheme is available. As shown in our previous study [68], it suffices inclining the straight wall with respect to the lattice to observe the breakdown of these calibrated solutions and the consequent inconsistency of the aforementioned "kinetic-based" LBM schemes as slip-flow models, i.e., they do not converge towards the physical slip condition when the mesh size tends to zero, regardless the calibration procedure employed. Additional evidence of this defect will be reported in this paper. For more details on this and other shortcomings we refer to Section IV of [68]. The other perspective adopted by the LBM community aims at modeling the slip velocity condition directly at LBM discrete level, i.e., without invoking any relationship to kinetic-based equations, e.g., Refs. [69–72]. So far, the LBM slip boundary schemes based on this reasoning have met partial success. Although for straight, lattice-aligned walls they are capable of supporting the slip velocity condition in a satisfactory manner, and exempt from calibration requirements [70], when applied to nonmesh aligned walls their performance seems more limited. That is, while they improve the consistency attained by kinetic-based schemes, their accuracy level never exceeds the first order in nonmesh aligned configurations, e.g., Refs. [69,71]. One of the objectives of this study is to point out the source of this limitation and to propose improved schemes that support the slip condition with second-order accuracy at arbitrary curved walls. To do so, we will follow the multireflection approach, originally developed by Ginzburg and coworkers [46,47] for no-slip walls, and extend it to the slip velocity condition. The choice behind the multireflection framework is twofold. First, for theoretical reasons, as the multireflection rests on a clear and precise working principle, the formulation of slip schemes can be executed rather straightforwardly, i.e., essentially through the same steps of the no-slip case, as explained in Appendix A of this manuscript. Second, for practical reasons, as this similitude can be explored by LBM users, particularly those already running LBM codes operating with no-slip multireflection schemes, as the extension to incorporate slip can be achieved with minimal changes, i.e., other than modifying the multireflection coefficients, the essence of the multireflection no-slip algorithm remains unchanged.

This work continues the study developed in Ref. [68] dedicated to the consistent LBM modeling of the slip-flow regime. In our early contribution [68], we have shown that the LBM provides a rather natural groundwork to model the slip-flow regime owing to the similarities between the closure relation of the LBM reflection-type boundary schemes, e.g., multireflection ones, and the "physical" slip velocity boundary condition, as both share a similar structure in terms of Taylor series of the fluid velocity at the wall. In this paper, we extend [68] with respect to the following three points. First, we demonstrate that the LBM closure relation, originally derived in Ref. [68] for the case of plane boundaries, also applies to curved walls. This equivalence is not *a priori* evident given that for curved surfaces the wall velocity slip depends on the shear stress, as given in Eq. (1), rather than the wall normal component of the velocity gradient alone, as originally considered in Ref. [68]. For illustration purposes, we limit this exposition to 2D geometries; yet the extension to 3D is straightforward. Second, we propose a strategy to preserve the numerical stability of the LBM slip boundary schemes, which may be impaired when slippage coefficients have large magnitude. In this respect, we also extend the modeling of low-speed (linear) Stokes flows, as considered in Ref. [68], to (nonlinear) Navier-Stokes flows. Third and final, we assess the conjecture made in Ref. [68] concerning the competitiveness of LBM as an effective CFD approach for the slip-flow regime. To this end, we compare the accuracy of different groups of slip boundary schemes operating on the LBM uniform mesh discretization against FEM simulations conducted on state-of-the-art body-fitted meshes. The LBM is implemented in our in-house code, while FEM is run with the COMSOL commercial code [73]. For the numerical tests we choose two classical fluid dynamics 2D problems, which are typically applied to the study of isothermal slippage phenomena over nonplanar surfaces, namely: (i) the cylindrical Couette flow [74–77] and (ii) the square array of circular cylinders crossed by a gaseous slow flow in the slip-flow regime [78–82]. Given that both benchmarks have been computed already within the LBM framework, namely case (i) by Refs. [67,71,83,84] and case (ii) by Refs. [71,82,85–87], the performance improvements of our LBM slip boundary schemes can be established more clearly. We note that the relevance of these tests goes beyond academic interest. They illustrate two application scenarios where the slip-flow theory has been receiving significant attention throughout the past few years, namely: case (i) for gas lubrication applications in microbearings [74–76]; and case (ii) for the shale gas exploitation in small pore size rocks [78–82].

The rest of the paper is organized as follows. Section II briefly presents the LBM scheme, operated on the basis of the two-relaxation-time (TRT) collision operator [47,88–92] and revises the relation between LBM and the target macroscopic hydrodynamic equations. Section III discusses the prescription of the slip velocity boundary condition over planar and curved surfaces. First, we revise the mathematical structure of these conditions, and second we demonstrate how they are approximated by generic reflection-type boundary schemes in LBM, according to their microscopic closure relations. Section IV addresses different classes of LBM reflection-type boundary schemes designed to model the slip velocity condition. In complement, we comment on the accuracy/consistency of low- and high-order LBM boundary schemes when approximating either no-slip or slip boundary conditions, and finalize with a discussion on the stability of these boundary schemes. Sections VI and VII contain the numerical results, where the main focus is given on the accuracy performance of LBM and FEM. Here, two benchmarks slip-flow problems are considered: the velocity profile of the cylindrical Couette flow in the slip-flow regime in Sec. VI; and the permeability measure of a slow rarefied gas crossing a periodic array of circular cylinders in the slip-flow regime in Sec. VII. Section VIII concludes the paper with a summary of the main results. The paper is further supplemented with two appendix sections. Appendix A

details the formulation of the parabolic slip schemes studied in this work, outlining the main steps in the derivation of the multireflection schemes [46,47]. Appendix B provides a complementary discussion on the reference solution adopted in Sec. VII.

II. TWO-RELAXATION-TIME LATTICE BOLTZMANN METHOD

The LBM [38–41] describes the evolution of populations $f_q(\vec{x},t)$, defined on space $\vec{x}$ and time t, along a discrete velocity set, called lattice, which features one immobile $\vec{c}_0=\vec{0}$ and $Q_m=Q-1$ nonzero velocity vectors $\vec{c}_q$ per grid node. The first $Q_m/2$ velocity vectors $\vec{c}_q$ are set diametrically opposite to the other $Q_m/2$ vectors $\vec{c}_{\bar{q}}=-\vec{c}_q$, where the pair $\{\vec{c}_q,\vec{c}_{\bar{q}}\}$ is referred to as a link. Here, we employ the d-dimensional lattice with Q velocities given by $d=2$ and $Q=9$, called $d2Q9$ model [39,41,93].

In terms of working principle, the LBM executes a succession of streaming and collision steps, Eqs. (2). The streaming step, Eq. (2a), performs a simple shift of populations to neighboring nodes. The collision step, Eq. (2b), is operated with the two-relaxation-time (TRT) model [41,47,88,89,91,92,94]. This collision model is constructed on the symmetry argument $\vec{c}_{\bar{q}}=-\vec{c}_q$. On this basis, populations are decomposed into symmetric $f_q^+=\frac{1}{2}(f_q+f_{\bar{q}})$ and antisymmetric $f_q^-=\frac{1}{2}(f_q-f_{\bar{q}})$ components, with immobile population $f_0^+=f_0$. Accordingly, the relaxation process is controlled by two collision eigenvalues, $\{s^+,s^-\}\in]0,2[$, for symmetric and antisymmetric modes, respectively [91,94]. They define two eigenfunctions $\Lambda^\pm=(\frac{1}{s^\pm}-\frac{1}{2})$, whose product $\Lambda=\Lambda^+\Lambda^-$ is known to control nondimensional steady-state solutions [47,89,90]. This structural invariance is the key element of the TRT scheme and what makes it a superior choice over the popular BGK scheme. The application of other LBM collision operators to the simulation of isothermal, low-speed flows in the slip-flow regime have been discussed in Appendix A of Ref. [68].

The update rule of the TRT-LBM [47,88,89], for streaming and collision steps, reads:

$$f_q(\vec{x}+\vec{c}_q,t+1)=\tilde{f}_q(\vec{x},t),\quad q=0,1,...,Q-1, \tag{2a}$$

$$\begin{aligned}\tilde{f}_q(\vec{x},t)&=[f_q+g_q^+ +g_q^-](\vec{x},t),\quad q=0,1,...,\frac{Q_m}{2},\\ \tilde{f}_{\bar{q}}(\vec{x},t)&=[f_{\bar{q}}+g_q^+ -g_q^-](\vec{x},t),\quad q=1,...,\frac{Q_m}{2},\end{aligned} \tag{2b}$$

where $\tilde{f}_q$ denotes the post-collision state of populations f_q, with $g_q^\pm=-s^\pm(f_q^\pm-e_q^\pm)$.

We consider the modeling of Navier-Stokes equations (NSE), with the force density $\vec{F}$. In the TRT scheme the NSE equilibrium [47,88] may be written as

$$e_q^+=P_q^\star+E_q^\star, \tag{3a}$$

$$e_q^-=j_q^\star+\Lambda^- F_q^\star, \tag{3b}$$

where

$$\begin{aligned}&P_q^\star=t_q^\star P,\quad P=c_s^2\rho,\quad e_0^+=e_0=\rho-2\sum_{q=1}^{Q_m/2}e_q^+,\\ &j_q^\star=t_q^\star j_q,\quad j_q=\vec{c}_q\cdot\vec{j},\quad F_q^\star=t_q^\star F_q,\quad F_q=\vec{c}_q\cdot\vec{F},\\ &E_q^\star=t_q^\star\frac{3\,j_q^2-\|\vec{j}\|^2}{2\bar{\rho}}.\end{aligned} \tag{4}$$

Note that several equivalent procedures exist to add forces in LBM as discussed in Sec. 2.2 of Ref. [47]. Here, we choose to include $\vec{F}$ inside the equilibrium, as given by Eq. (3b), in line with past studies [47,88,89]. This choice helps simplifying the theoretical derivations, as sketched in Appendix A. As for the equilibrium, we adopt the incompressible model [95,96], where density is split into an arbitrary ground state density $\bar{\rho}=$ constant and a varying mass density field ρ. The c_s^2 in the equation of state $P=c_s^2\rho$ is a free parameter, limited by stability bounds, e.g., $c_s^2\in]0,\frac{3}{5}]$ in the d2Q9 [91,92]. Additionally, $t_q^\star$ refers to isotropic hydrodynamic weights [39,41,93], with $\{t_q^{\star(I)},t_q^{\star(II)}\}=\{\frac{1}{3},\frac{1}{12}\}$ in the d2Q9 model. These lattice weights cope with the two constraints for standard lattices: $2\sum_{q=1}^{Q_m/2}t_q^\star c_{q\alpha}c_{q\beta}=\delta_{\alpha\beta}$ and $6\sum_{q=1}^{Q_m/2}t_q^\star c_{q\alpha}^2c_{q\beta}^2=1+2\delta_{\alpha\beta}$, where $\delta_{\alpha\beta}$ is the Kronecker δ.

The LBM solves for the macroscopic quantities, mass density ρ, and momentum density $\vec{j}$, through the zeroth- and first-order velocity moments, determined on f_q^+ and f_q^-, respectively, as follows:

$$\begin{aligned}&\rho=f_0+2\sum_{q=1}^{Q_m/2}f_q^+,\quad \vec{J}=2\sum_{q=1}^{Q_m/2}f_q^-\vec{c}_q,\quad \vec{F}=2\sum_{q=1}^{Q_m/2}F_q\vec{c}_q,\\ &\vec{j}=\vec{J}+\frac{1}{2}\vec{F}.\end{aligned} \tag{5}$$

The macroscopic conservation laws for the mass and momentum balance are established by

$$\sum_{q=0}^{Q-1}g_q^+=0, \tag{6a}$$

$$2\sum_{q=1}^{Q_m/2}g_q^-\vec{c}_q=\vec{F}. \tag{6b}$$

The explicit form of the macroscopic conservation laws can be determined through the second-order Chapman-Enskog expansion method [38,46,89,95]. Based on this procedure the steady-state structure of the nonequilibrium post-collision quantities $g_q^\pm$ can be proven [89] to be

$$g_q^\pm=\partial_q(e_q^\mp-\Lambda^\mp\partial_q e_q^\pm)+O(\epsilon^3), \tag{7}$$

where $\partial_q=\vec{c}_q\cdot\vec{\nabla}$ expresses the lattice-projected directional derivative. In this study $\Lambda^\pm$ is held spatially uniform.

Then, if we substitute Eqs. (7) into Eqs. (6), and take into account the form of equilibrium, Eqs. (3) and (4), together with the definitions of the velocity moments, given in Eq. (5), we

arrive at the expected steady-state incompressible NSE:

$$\vec{\nabla}\cdot\vec{u}=0,\quad \vec{u}=\frac{\vec{j}}{\bar{\rho}}, \tag{8a}$$

$$\vec{\nabla}\cdot(\vec{u}\otimes\vec{u})=\frac{1}{\bar{\rho}}(\vec{F}-\vec{\nabla}P)+\nu\Delta\vec{u},\quad \nu=\frac{1}{3}\Lambda^{+}, \tag{8b}$$

where the second-order derivatives of pressure and nonlinear terms have been neglected in consistency with the second-order scaling of the Chapman-Enskog expansion [38,46].

Remark. The Chapman-Enskog expansion unfolds the content of the nonequilibrium quantities, through a perturbative approximation method, controlled by the ϵ smallest parameter [38,46,89,95]. It is important to note that, in the LBM context, the ϵ parameter expresses the ratio of the lattice unit to the characteristic length scale of the problem [47,68,88,95], and shall not be confused with the Kn number [58,61,63,66]. That is, while ϵ is a grid scale parameter, Kn is a nondimensional group that controls the problem physical regime. By conducting the second-order Chapman-Enskog analysis, the procedure consists of substituting Eqs. (8) into Eqs. (6), with assumption $|\vec{F}|=O(\epsilon)$ [41,97–99], so that we end up recovering Eqs. (8) with a $O(\epsilon^2)$ residue. This means the error in the LBM approximation toward the intended PDE system is second-order in the mesh spacing [89,90]. Along these lines, higher-order terms in ϵ shall be interpreted as the truncation terms in the numerical model, rather than related to physically based Kn corrections to the NSE framework. In other words, they do *not* describe Burnett or super-Burnett fluxes [100], but simply the discretization errors brought with the numerical approximation.

III. SLIP VELOCITY BOUNDARY CONDITION

A. Hydrodynamic theory: Boundary closure relations

In this section we briefly revise the structure of the slip velocity boundary condition. To begin with, let us outline the main working hypotheses taken in the course of this study. In bulk, we assume a single component fluid under isothermal conditions, with Newtonian stress tensor given by $\tau_{ij}=\mu(\frac{\partial u_i}{\partial x_j}+\frac{\partial u_j}{\partial x_i})$. At boundaries, we assume a smooth solid surface (i.e., corners are excluded) with rigid and impermeable walls that may undergo a solid-body motion with velocity $\vec{u}_w$. As for the fluid-wall interaction, we assume a slip velocity model according to Eq. (1). Altogether, the boundary conditions for the normal and the tangential fluid velocity components read

$$\left(u_i-u_{w_i}\right)n_i=0, \tag{9a}$$

$$\left(u_i-u_{w_i}\right)t_i=-\mathcal{C}\,\lambda\left(\frac{\partial u_i}{\partial x_j}+\frac{\partial u_j}{\partial x_i}\right)n_i\,t_j. \tag{9b}$$

Here, Einstein tensorial notation is employed, with repeated indices implying summation, e.g., $u_it_i=\sum_i u_it_i=\vec{u}\cdot\vec{t}$. As for sign convention, we define $\vec{n}$ to be the normal unit vector, pointing along the wall normal outward direction (which explains the minus sign here) and $\vec{t}$ the tangent unit vector, pointing along the positive axis of the coordinate system.

Our objective is to investigate under which circumstances a boundary rule formulated in LBM is capable of approximating Eqs. (9) within the same level of accuracy of the LBM approximation of the NSE in bulk, as discussed in Sec. II. We note that this question has been the subject of past studies concerning the operation of the no-slip velocity condition [41,46,101,102]. Yet, the numerical implementation of Eqs. (9) brings new additional challenges. First, compared to the no-slip case, which prescribes a Dirichlet (specified value) boundary condition, the slip condition is of Robin-type, Eq. (9b), which requires dealing with the relation between the boundary value and its gradient. Second, since the normal velocity condition remains of Dirichlet-type, Eq. (9a), the numerical boundary model must be able to deal with the different mathematical nature of each velocity component simultaneously, whereas in the no-slip case both velocity components are of Dirichlet-type at the boundary. These two issues will be addressed next.

For the sake of illustration, let us consider the slip velocity boundary condition, Eqs. (9), at two particular 2D coordinate systems.

(1) The Cartesian coordinate system $\vec{x}\mapsto(s,n)$, whose components s and n locally align to the surface tangential and normal vectors, respectively. That is, $t_i=\mathbf{i}_s$ and $n_j=-\mathbf{i}_n$, so that Eqs. (9) become

$$u_n-u_{w_n}=0, \tag{10a}$$

$$u_s-u_{w_s}=\mathcal{C}\,\lambda\left(\frac{\partial u_s}{\partial n}+\frac{\partial u_n}{\partial s}\right). \tag{10b}$$

(2) The polar coordinate system $\vec{x}\mapsto(r,\theta)$, whose components r and θ locally align to the surface normal and tangential vectors, respectively. That is, $t_i=\mathbf{i}_\theta$ and $n_j=-\mathbf{i}_r$, so that Eqs. (9) become

$$u_r-u_{w_r}=0, \tag{11a}$$

$$u_\theta-u_{w_\theta}=\mathcal{C}\,\lambda\left(\frac{\partial u_\theta}{\partial r}-\frac{u_\theta}{r}\right). \tag{11b}$$

B. Lattice Boltzmann theory: Boundary closure relations

In standard LBM the geometry is discretized on an uniform Cartesian mesh. Consequently, arbitrary boundaries will necessarily fall outside the lattice nodes. This demands the careful characterization of the nodes inside the fluid domain, where two groups of nodes can be identified [41]: (i) *Fluid nodes* which are sites where the LBM update rule, Eq. (2), applies; (ii) *Boundary nodes* $\vec{x}_\mathrm{b}$ which are sites also belonging to the fluid region but with, at least, one link connected to the solid domain, i.e., $\vec{x}_\mathrm{b}+\vec{c}_q\in$ solid; see Fig. 1. For that reason, the solution at boundary nodes must undergo a different update rule, as will be addressed in Sec. IV and derived in Appendix A. With the knowledge of the wall cut-link distance δ_q, the wall location gets determined as $\vec{x}_\mathrm{w}=\vec{x}_\mathrm{b}+\vec{c}_q\,\delta_q$; see Fig. 1. Below, we will examine the structure of the LBM closure relation set by generic linkwise boundary schemes and how this closure relation approximates the slip velocity boundary conditions given by Eqs. (10) or (11); the way to recover this closure relation with typical multireflection schemes [46,47,68] is deferred to Appendix A.

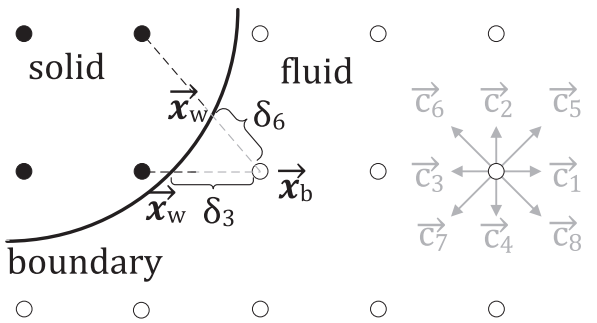

FIG. 1. Discretization of a curved wall on the uniform mesh of the LBM operating on d2Q9 lattice.

We consider a generic linkwise LBM boundary scheme operating at $\vec{x}_b$ and assume it obeys the LBM closure relation for the slip velocity boundary condition applied at $\vec{x}_w$ (recall, $\vec{x}_w = \vec{x}_b + \vec{c}_q\,\delta_q$) in terms of the Taylor-type approximation along each wall-cut link q, according to Ref. [68]:

$$
\begin{aligned}
& j_q(\vec{x}_b) + \alpha_q^+\,\partial_q j_q(\vec{x}_b) + \alpha_q^-\,\partial_q^2 j_q(\vec{x}_b) + O(\epsilon^3) = j_{q\,w}(\vec{x}_w), \\
& \alpha_q^+ := (\delta_q + \mathcal{C}\,\lambda_q), \quad \alpha_q^- := \left(\frac{\delta_q^2}{2} + \mathcal{C}\,\lambda_q\,\delta_q\right), \\
& \lambda_q := \frac{\lambda}{\Theta_q}, \quad \Theta_q := (\vec{c}_q\cdot\vec{n}), \quad \vec{x}_w = \vec{x}_b + \vec{c}_q\,\delta_q.
\end{aligned}
\tag{12}
$$

Note, the coefficients α_q^+ and α_q^- may also depend on the spatial location $\vec{x}_b$ (besides the linkwise dependence q already expressed); yet, to alleviate notation, this $\vec{x}_b$ dependence on $\alpha_q^\pm$ will be omitted throughout the manuscript.

Next, we will demonstrate that Eq. (12) contains both the Robin- and Dirichlet-type velocity boundary condition components, as reported in Sec. III A, and it approximates them as a second-order Taylor series about point $\vec{x}_b$ with the wall cut-link distance δ_q as increment. This proof will be sketched below for a 2D geometry, considering plane and curved boundaries separately; the 3D extension is straightforward.

1. Plane boundaries

The case of plane boundaries is more conveniently dealt with in a Cartesian coordinate system. On this basis, the LBM closure relation given by Eq. (12) writes as follows:

$$
\begin{aligned}
& (c_{qs}\,j_s + c_{qn}\,j_n) + (\delta_q + \mathcal{C}\,\lambda_q)\left[c_{qs}^2\frac{\partial j_s}{\partial s} + c_{qs}c_{qn}\left(\frac{\partial j_s}{\partial n} + \frac{\partial j_n}{\partial s}\right) + c_{qn}^2\frac{\partial j_n}{\partial n}\right] + \left(\frac{\delta_q^2}{2} + \mathcal{C}\,\lambda_q\,\delta_q\right) \\
& \times\left[c_{qs}^3\frac{\partial^2 j_s}{\partial s^2} + c_{qs}^2c_{qn}\left(\frac{\partial^2 j_n}{\partial s^2} + 2\,\frac{\partial^2 j_s}{\partial s\partial n}\right) + c_{qs}c_{qn}^2\left(\frac{\partial^2 j_s}{\partial n^2} + 2\,\frac{\partial^2 j_n}{\partial s\partial n}\right) + c_{qn}^3\frac{\partial^2 j_n}{\partial n^2}\right] + O(\epsilon^3) = c_{qs}\,j_{w_s} + c_{qn}\,j_{w_n}.
\end{aligned}
\tag{13}
$$

It is useful to reorganize Eq. (13) into tangential and normal components:

$$
\begin{aligned}
& c_{qs}\underbrace{\left[j_s + (\delta_n + \mathcal{C}\,\lambda)\left(\frac{\partial j_s}{\partial n} + \frac{\partial j_n}{\partial s}\right) + \left(\frac{\delta_n^2}{2} + \mathcal{C}\,\lambda\,\delta_n\right)\left(\frac{\partial^2 j_s}{\partial n^2} + \frac{\partial^2 j_n}{\partial s\partial n}\right) - j_{w_s}\right]}_{=2^{\text{nd}}-\text{order Taylor Expansion of Eq.}(10b)} + c_{qn}\underbrace{\left[j_n + \delta_n\frac{\partial j_n}{\partial n} + \frac{\delta_n^2}{2}\frac{\partial^2 j_n}{\partial n^2} - j_{w_n}\right]}_{=2^{\text{nd}}-\text{order Taylor Expansion of Eq.}(10a)} \\
& + \text{Error} = 0.
\end{aligned}
\tag{14}
$$

Above, we have used the definitions $\Theta_q := c_{qn}$ and $\delta_n := \delta_q\,c_{qn}$. Furthermore, the Error in Eq. (14) is given by

$$
\begin{aligned}
\text{Error} = {} & c_{qs}\left[(\delta_q + \mathcal{C}\,\lambda_q)c_{qs}\frac{\partial j_s}{\partial s} + \left(\frac{\delta_q^2}{2} + \mathcal{C}\,\lambda_q\,\delta_q\right)\left(c_{qs}^2\frac{\partial^2 j_s}{\partial s^2} + c_{qn}^2\frac{\partial^2 j_n}{\partial s\partial n}\right)\right] \\
& + c_{qn}\left[\mathcal{C}\,\lambda_q\,c_{qn}\frac{\partial j_n}{\partial n} + (\mathcal{C}\,\lambda_q\,\delta_q)c_{qn}^2\frac{\partial^2 j_n}{\partial n^2} + \left(\frac{\delta_q^2}{2} + \mathcal{C}\,\lambda_q\,\delta_q\right)c_{qs}^2\left(\frac{\partial^2 j_n}{\partial s^2} + 2\,\frac{\partial^2 j_s}{\partial s\partial n}\right)\right] + O(\epsilon^3).
\end{aligned}
\tag{15}
$$

Clearly, to guarantee that Eq. (14) reproduces Eq. (10) as a second-order Taylor series approximation, the residue in Eq. (15) must be reduced to Error $= O(\epsilon^3)$. Yet, to satisfy this condition a few estimates must be invoked. The first one refers to the state of slip at the boundary, which shall be constant or otherwise not too far from this condition. The use of this assumption is not an exclusive from our approach, e.g., Reis and Dellar [70] have also used it when formulating their LBM slip boundary schemes (cf. Sec. V in Ref. [70]). We note that, while theoretically this assumption may appear too restrictive, our numerical results (alongside with those reported in Ref. [70]) confirm that accurate solutions can still be reached, even at more general slip scenarios, providing slip variations are slow. The satisfaction with the constant slip velocity condition permits establishing $\frac{\partial j_s}{\partial s} = 0$ along the plane wall. The second approximation is more general and refers to the fact that the boundary condition is prescribed at $\vec{x}_w$ while Eq. (15) applies at $\vec{x}_b$, where the difference is $(\vec{x}_b - \vec{x}_w)\cdot\vec{n} = \delta_n$. For general flows, and bearing in mind that we have assumed a smooth boundary, the difference between evaluating $\frac{\partial j_s}{\partial s}$ at $\vec{x}_b$ rather than at $\vec{x}_w$ is small. Therefore, we may still conjecture $\frac{\partial j_s}{\partial s} = 0$, which is an approximation ubiquitous to linkwise boundary schemes, even those concerned with the no-slip condition, e.g., Refs. [42,43,45,46]. Obviously, in the case of streamwise invariant flows, the condition $\frac{\partial j_s}{\partial s} = 0$ becomes exact, a result that also comprises the constant slip condition. In fact, these two approximations end up being somehow related. Assuming their validity, we work out the $\frac{\partial j_s}{\partial s} = 0$ assumption together with the flow incompressibility condition to establish the

additional simplifications: $\frac{\partial j_n}{\partial n} = -\frac{\partial j_s}{\partial s} = 0$, $\frac{\partial^2 j_n}{\partial s \partial n} = -\frac{\partial^2 j_s}{\partial s^2} = 0$ and $\frac{\partial^2 j_s}{\partial s \partial n} = -\frac{\partial^2 j_n}{\partial n^2} = 0$. Everything considered, the closure relation given by Eq. (12) is proven to prescribe the slip velocity condition at plane walls in the following form:

$$c_{qs}\left[j_s + (\delta_n + \mathcal{C}\,\lambda)\,\frac{\partial j_s}{\partial n} + \left(\frac{\delta_n^2}{2} + \mathcal{C}\,\lambda\,\delta_n\right)\frac{\partial^2 j_s}{\partial n^2} - j_{w_s}\right] + c_{qn}\left[j_n + \delta_n\,\frac{\partial j_n}{\partial n} + \frac{\delta_n^2}{2}\,\frac{\partial^2 j_n}{\partial n^2} - j_{w_n}\right] + O(\epsilon^3) = 0. \tag{16}$$

Equation (16) corresponds to the second-order Taylor series approximation, about $\vec{x}_\mathrm{b}$ with increment δ_n, of the slip condition previously developed in [68], referring to planar walls. Equation (16) reveals that for a wall-cut link where the LBM boundary scheme satisfies Eq. (12), then both the Robin-type boundary condition in the tangential component and the Dirichlet-type boundary condition in the normal component, see Eq (10), are established within the same level of accuracy.

2. Curved boundaries

The case of curved walls is more involving. Here, it is convenient to express Eq. (12) in the polar coordinate system:

$$\begin{aligned}
&(c_{q\theta}\,j_\theta + c_{qr}\,j_r) + (\delta_q + \mathcal{C}\,\lambda_q)\left[c_{q\theta}^2\left\{\frac{1}{r}\frac{\partial j_\theta}{\partial\theta} + \frac{j_r}{r}\right\} + c_{q\theta}c_{qr}\left(\frac{\partial j_\theta}{\partial r} + \left\{\frac{1}{r}\frac{\partial j_r}{\partial\theta} - \frac{j_\theta}{r}\right\}\right) + c_{qr}^2\,\frac{\partial j_r}{\partial r}\right] + \left(\frac{\delta_q^2}{2} + \mathcal{C}\,\lambda_q\,\delta_q\right)\\
&\times\left[c_{q\theta}^3\left\{\frac{1}{r^2}\frac{\partial^2 j_\theta}{\partial\theta^2} + \frac{2}{r^2}\frac{\partial j_r}{\partial\theta} + \frac{1}{r}\frac{\partial j_\theta}{\partial r} - \frac{j_\theta}{r^2}\right\} + c_{q\theta}^2 c_{qr}\left(\left\{\frac{1}{r^2}\frac{\partial^2 j_r}{\partial\theta^2} + \frac{1}{r}\frac{\partial j_r}{\partial r} - \frac{2}{r^2}\frac{\partial j_\theta}{\partial\theta} - \frac{j_r}{r^2}\right\}\right.\right.\\
&\left.\left. + \left\{\frac{2}{r}\frac{\partial^2 j_\theta}{\partial r\partial\theta} - \frac{2}{r^2}\frac{\partial j_\theta}{\partial\theta} + \frac{2}{r}\frac{\partial j_r}{\partial r} - \frac{2j_r}{r^2}\right\}\right) + c_{q\theta}c_{qr}^2\left(\frac{\partial^2 j_\theta}{\partial r^2} + \left\{\frac{2}{r}\frac{\partial^2 j_r}{\partial r\partial\theta} - \frac{2}{r}\frac{\partial j_\theta}{\partial r} - \frac{2}{r^2}\frac{\partial j_r}{\partial\theta} + \frac{2j_\theta}{r^2}\right\}\right) + c_{qr}^3\,\frac{\partial^2 j_r}{\partial r^2}\right]\\
&+ O(\epsilon^3) = c_{q\theta}\,j_{w_\theta} + c_{qr}\,j_{w_r},
\end{aligned} \tag{17}$$

where $\lambda_q := (\vec{c}_q \cdot \vec{n}) = \lambda/\Theta_q$, with $\Theta_q := c_{qr}$. Once again, it is useful to reorganize Eq. (17) into circumferential and radial components:

$$\begin{aligned}
&c_{q\theta}\left[j_\theta + (\delta_r + \mathcal{C}\,\lambda)\left(\frac{\partial j_\theta}{\partial r} + \left\{\frac{1}{r}\frac{\partial j_r}{\partial\theta} - \frac{j_\theta}{r}\right\}\right) + \left(\frac{\delta_r^2}{2} + \mathcal{C}\,\lambda\,\delta_r\right)\left(\frac{\partial^2 j_\theta}{\partial r^2} + \left\{\frac{1}{r}\frac{\partial^2 j_r}{\partial r\partial\theta} - \frac{1}{r}\frac{\partial j_\theta}{\partial r} - \frac{1}{r^2}\frac{\partial j_r}{\partial\theta} + \frac{j_\theta}{r^2}\right\}\right) - j_{w_\theta}\right]\\
&+ c_{qr}\left[j_r + \delta_r\,\frac{\partial j_r}{\partial r} + \frac{\delta_r^2}{2}\,\frac{\partial^2 j_r}{\partial r^2} - j_{w_r}\right] + \text{Error} = 0,
\end{aligned} \tag{18}$$

where $\delta_r := \delta_q\,c_{qr}$ and the Error is given by

$$\begin{aligned}
\text{Error} = {}& c_{q\theta}\left[(\delta_q + \mathcal{C}\,\lambda_q)c_{q\theta}\left\{\frac{1}{r}\frac{\partial j_\theta}{\partial\theta} + \frac{j_r}{r}\right\} + \left(\frac{\delta_q^2}{2} + \mathcal{C}\,\lambda_q\,\delta_q\right)\left(c_{q\theta}^2\left\{\frac{1}{r^2}\frac{\partial^2 j_\theta}{\partial\theta^2} + \frac{2}{r^2}\frac{\partial j_r}{\partial\theta} + \frac{1}{r}\frac{\partial j_\theta}{\partial r} - \frac{j_\theta}{r^2}\right\}\right.\right.\\
&\left.\left. + c_{qr}^2\left\{\frac{1}{r}\frac{\partial^2 j_r}{\partial r\partial\theta} - \frac{1}{r}\frac{\partial j_\theta}{\partial r} - \frac{1}{r^2}\frac{\partial j_r}{\partial\theta} + \frac{j_\theta}{r^2}\right\}\right)\right] + c_{qr}\left[\mathcal{C}\,\lambda_q\,c_{qr}\,\frac{\partial j_r}{\partial r} + (\mathcal{C}\,\lambda_q\,\delta_q)\,c_{qr}^2\,\frac{\partial^2 j_r}{\partial r^2} + \left(\frac{\delta_q^2}{2} + \mathcal{C}\,\lambda_q\,\delta_q\right)\right.\\
&\left.\times\,c_{q\theta}^2\left(\left\{\frac{1}{r^2}\frac{\partial^2 j_r}{\partial\theta^2} + \frac{1}{r}\frac{\partial j_r}{\partial r} - \frac{2}{r^2}\frac{\partial j_\theta}{\partial\theta} - \frac{j_r}{r^2}\right\} + \left\{\frac{2}{r}\frac{\partial^2 j_\theta}{\partial r\partial\theta} - \frac{2}{r^2}\frac{\partial j_\theta}{\partial\theta} + \frac{2}{r}\frac{\partial j_r}{\partial r} - \frac{2j_r}{r^2}\right\}\right)\right] + O(\epsilon^3).
\end{aligned} \tag{19}$$

The last step consists in demonstrating that Eq. (18) corresponds to the second-order Taylor expansion of Eq. (11), which is equivalent to demonstrating that Eq. (19) reduces to Error $= O(\epsilon^3)$. This is proven by invoking the same kind of assumptions adopted in the plane wall case, in particular the constant slip velocity condition. When transcribed to the curved boundary case, these assumptions lead to $\frac{\partial j_\theta}{\partial\theta} = 0$ along the curved wall. Based on this result, the analysis proceeds with the flow incompressibility condition: $\frac{\partial j_r}{\partial r} + \frac{1}{r}\frac{\partial j_\theta}{\partial\theta} + \frac{j_r}{r} = 0$, which permits working out in polar coordinates the equivalent of the conditions $\frac{\partial j_n}{\partial n} = -\frac{\partial j_s}{\partial s} = 0$, $\frac{\partial^2 j_n}{\partial s\partial n} = -\frac{\partial^2 j_s}{\partial s^2} = 0$ and $\frac{\partial^2 j_s}{\partial s\partial n} = -\frac{\partial^2 j_n}{\partial n^2} = 0$, as follows: $(\frac{\partial j_r}{\partial r} + \frac{j_r}{r}) = -\frac{1}{r}\frac{\partial j_\theta}{\partial\theta} = 0$, $(\frac{1}{r}\frac{\partial^2 j_r}{\partial r\partial\theta} - \frac{1}{r}\frac{\partial j_\theta}{\partial r} - \frac{1}{r^2}\frac{\partial j_r}{\partial\theta} + \frac{j_\theta}{r^2}) = -(\frac{1}{r^2}\frac{\partial^2 j_\theta}{\partial\theta^2} + \frac{2}{r^2}\frac{\partial j_r}{\partial\theta} + \frac{1}{r}\frac{\partial j_\theta}{\partial r} - \frac{j_\theta}{r^2}) = 0$ and $(\frac{1}{r}\frac{\partial^2 j_\theta}{\partial r\partial\theta} - \frac{1}{r^2}\frac{\partial j_\theta}{\partial\theta} + \frac{1}{r}\frac{\partial j_r}{\partial r} - \frac{j_r}{r^2}) = -\frac{\partial^2 j_r}{\partial r^2} = 0$, respectively. The substitution of these results into Eq. (19) leads to the conclusion that, indeed, Error $= O(\epsilon^3)$. Everything considered, Eq. (18) simplifies to

$$\begin{aligned}
&c_{q\theta}\underbrace{\left[j_\theta + (\delta_r + \mathcal{C}\,\lambda)\left(\frac{\partial j_\theta}{\partial r} - \frac{j_\theta}{r}\right) + \left(\frac{\delta_r^2}{2} + \mathcal{C}\,\lambda\,\delta_r\right)\left(\frac{\partial^2 j_\theta}{\partial r^2} - \frac{1}{r}\frac{\partial j_\theta}{\partial r} + \frac{j_\theta}{r^2}\right) - j_{w_\theta}\right]}_{=2^{\text{nd}}-\text{order Taylor Expansion of Eq.(11}b\text{)}} + c_{qr}\underbrace{\left[j_r + \delta_r\,\frac{\partial j_r}{\partial r} + \frac{\delta_r^2}{2}\,\frac{\partial^2 j_r}{\partial r^2} - j_{w_r}\right]}_{=2^{\text{nd}}-\text{order Taylor Expansion of Eq.(11}a\text{)}}\\
&+ O(\epsilon^3) = 0.
\end{aligned} \tag{20}$$

Equation (20) proves that the LBM closure relation, Eq. (12), indeed satisfies the slip velocity condition at curved walls, Eq. (11), as a second-order Taylor series approximation, about $\vec{x}_\mathrm{b}$ with increment δ_r, of the Robin-type boundary condition in the circumferential component and the Dirichlet-type boundary condition in the radial component. The above theoretical conclusions will be numerically verified in Secs. VI and VII.

TABLE II. LBM boundary schemes: coefficients of interpolation together with correction parameters $F_q^{\text{p.c.}}$ and $\alpha^{(u)}$ in Eq. (21), where coefficients are $\alpha_q^+ := (\delta_q + \mathcal{C}\,\lambda_q)$ and $\alpha_q^- := (\frac{\delta_q^2}{2} + \mathcal{C}\,\lambda_q\,\delta_q)$. When the slippage correction vanishes, the $\alpha_q^\pm$ coefficients take the form of the no-slip schemes previously reported in Refs. [46,47].

	Kinetic schemes	Linear schemes			Parabolic schemes		
	DBB	CLI slip	MGULI slip	MGDLI slip	MR(k_q) slip	MR1 slip	MGMR(C) slip
κ_1	$\frac{3\nu-\mathcal{C}\lambda}{3\nu+\mathcal{C}\lambda}$	1	$2\alpha_q^+$	$\frac{1}{2\alpha_q^+}$	$\frac{2\alpha_q^+ + 2\alpha_q^- - k_q}{1+k_q}$	1	$\frac{1+2\alpha_q^+ + 2\alpha_q^- + 2C\Lambda^-}{1+2\alpha_q^+ + 2\alpha_q^- - 2C\Lambda^-}$
κ_0	0	$\frac{1-2\alpha_q^+}{1+2\alpha_q^+}$	$1-\kappa_1$	0	$\frac{\frac{3}{2} - 3\alpha_q^+ - 4\alpha_q^- + 2k_q}{1+k_q}$	$\frac{1-2\alpha_q^+ - 4\alpha_q^-}{1+2\alpha_q^+ + 2\alpha_q^-}$	$\frac{1-2\alpha_q^+ - 4\alpha_q^- - 4C\Lambda^-}{1+2\alpha_q^+ + 2\alpha_q^- - 2C\Lambda^-}$
$\bar{\kappa}_{-1}$	0	$-\kappa_0$	0	$1-\kappa_1$	$\frac{\frac{1}{2} - \alpha_q^+ + 2k_q}{1+k_q}$	$-\kappa_0$	$\frac{-1+2\alpha_q^+ + 4\alpha_q^- - 4C\Lambda^-}{1+2\alpha_q^+ + 2\alpha_q^- - 2C\Lambda^-}$
κ_{-1}	0	0	0	0	$\frac{-\frac{1}{2} + \alpha_q^+ + 2\alpha_q^- - k_q}{1+k_q}$	$\frac{2\alpha_q^-}{1+2\alpha_q^+ + 2\alpha_q^-}$	$\frac{2\alpha_q^- + 2C\Lambda^-}{1+2\alpha_q^+ + 2\alpha_q^- - 2C\Lambda^-}$
$\bar{\kappa}_{-2}$	0	0	0	0	$\frac{-\frac{1}{2} + \alpha_q^+ - k_q}{1+k_q}$	$-\kappa_{-1}$	$\frac{-2\alpha_q^- + 2C\Lambda^-}{1+2\alpha_q^+ + 2\alpha_q^- - 2C\Lambda^-}$
$\alpha^{(u)}$	$2\,\kappa_1$	$\frac{4}{1+2\alpha_q^+}$	2	$1-\kappa_1$	$\frac{2}{1+k_q}$	$\frac{4}{1+2\alpha_q^+ + 2\alpha_q^-}$	$\frac{4}{1+2\alpha_q^+ + 2\alpha_q^- - 2C\Lambda^-}$
$F_q^{\text{p.c.}}$	$(1-\kappa_1)\,e_q(\rho_w, \vec{j}_w)$		$(1-\kappa_1)g_q^-$			$\alpha^{(u)}\Lambda^-(g_q^- - F_q^\star)$	

IV. SLIP VELOCITY BOUNDARY SCHEMES IN LBM

In LBM, the problem with the implementation of boundary conditions boils down to finding the post-streaming state of incoming boundary populations which reproduces the intended hydrodynamic boundary condition, up to the desired accuracy. A natural way to accomplish this goal is through some suitable linear combination of known populations so that the boundary update rule matches the target closure relation, here given by Eq. (12). To execute this task, we will consider three classes of boundary schemes, called: kinetic, linear, and parabolic schemes. They represent a trade-off between complexity and accuracy, as explained ahead.

Now, we briefly revise the operation principle underlying these LBM boundary schemes. Let us consider the boundary node $\vec{x}_b$, where $\vec{x}_b + \vec{c}_q$ is a solid node and $\vec{x}_b - \vec{c}_q$ is the nearest fluid node. We propose to implement the slip boundary condition following the generic boundary update rule:

$$\begin{aligned} f_{\bar{q}}(\vec{x}_b, t+1) = {} & \kappa_1 \tilde{f}_q(\vec{x}_b, t) + \bar{\kappa}_{-1}\tilde{f}_{\bar{q}}(\vec{x}_b, t) + \kappa_0 f_q(\vec{x}_b, t+1) \\ & + \kappa_{-1} f_q(\vec{x}_b - \vec{c}_q, t+1) + \bar{\kappa}_{-2}\tilde{f}_{\bar{q}}(\vec{x}_b - \vec{c}_q, t) \\ & + F_q^{\text{p.c.}}(\vec{x}_b, t) - \alpha^{(u)} j^\star_{q\,w}(\vec{x}_w, t), \end{aligned} \tag{21}$$

with

$$j^\star_{q\,w} = t_q^\star\, j_{q\,w}, \quad j_{q\,w} = \vec{c}_q \cdot \vec{j}_w. \tag{22}$$

The structure of Eq. (21) follows the general multireflection approach [46,47]. Here, for convenience, the unknown incoming boundary populations, specified after propagation, are determined through the linear combination of the known post-collision populations evaluated at time step t and the known outgoing populations evaluated at the state after the propagation step, i.e., at time step $t+1$. This form of multireflection algorithm employs the same structure of the standard no-slip multireflection one [46–48,68]. Namely, it consists of the interpolation coefficients $\{\kappa_1, \kappa_0, \bar{\kappa}_{-1}, \kappa_{-1}, \bar{\kappa}_{-2}\}$ further supplemented by the correction parameters $F_q^{\text{p.c.}}$ and $\alpha^{(u)}$ with the Dirichlet correction $j^\star_{q\,w}$ given by Eq. (22). The form of these terms for the slip boundary case and the different classes of slip boundary schemes considered herein is detailed in Table II; they all reduce to known no-slip formulas when the slippage contribution vanishes. Below, we will discuss how accurate they prescribe the no-slip and the slip velocity conditions at arbitrarily curved walls. Other geometrical features, such as corners, are not addressed in this work. For those special sites, as preliminary approach, we suggest the use of the no-slip condition, e.g., by means of the local boundary rule given by Eq. (5.26) in Ref. [47].

A. Parabolic schemes

Parabolic schemes make full use of Eq. (21). Thereby, they operate in a nonlocal manner, requiring a two-node implementation. This disadvantage is strongly compensated by their ability to reproduce the slip closure relation given by Eq. (12). As a result, parabolic schemes support the *second-order accuracy* of the LBM in both no-slip and slip boundary problems. Moreover, their operation principle is consistent with the bulk TRT invariance property, popularized in LBM jargon as the "viscosity-independent" property [90], cf. Sec. II. This feature should not be taken for granted. By default, several interpolation-based LBM boundary schemes, e.g., Refs. [43–45,103], fail to satisfy this invariance property, even when running on the TRT framework

In terms of implementation, the family of parabolic schemes is chosen to be constructed through the multireflection (MR) formulation [46,47]. This choice takes advantage of the transparent working principle of the MR framework, making it readily applicable for our intents; derivations are sketched in Appendix A, more details are given in Refs. [46,47]. In Ref. [68], we have developed three different sets of MR coefficients for the slip case, namely: the general MR(k_q) family and the two particular cases MR1 and MGMR(C) subfamilies; they are displayed in Table II. The general parameter k_q recovers the MR1 and MGMR(C) schemes as follows: $k_q = (-\frac{1}{2} + \alpha_q^+ + \alpha_q^-)$ in MR1 and $k_q = (-\frac{1}{2} + \alpha_q^+ + \alpha_q^- - C\Lambda^-)$ in MGMR(C), where C and Λ^- are both free tunable. Notice that the free numerical coefficient C parametrizing

the MGMR(C) scheme should not be confused with $\mathcal{C}$ the physical slippage coefficient, which parameterizes the α_q^+ and α_q^- coefficients. While the role of these free numerical parameters views primarily stability purposes, they also lead to slight differences in terms of accuracy, due to $O(\epsilon^3)$ differences in the closure relations of the parabolic schemes. Yet, these differences are beyond the order of accuracy of this study. The ensemble of these topics is deferred for a future work. In this work, we will restrict the study of parabolic schemes to the simple MR1 slip scheme. From the structural standpoint, we outline that the input parameters of the slip parabolic schemes are α_q^+ and α_q^-, in agreement with the closure relation they support, Eq (12). Here, α_q^+ and α_q^- are only limited to the nonnegativity condition. Consequently, they may take arbitrarily large values, a feature that may impact the numerical stability of the LBM evolution process as will be discussed in Sec. V, where a general solution method will be proposed. We will distinguish with a ($\star$) indicator the parabolic schemes subjected to a stabilization treatment.

B. Linear schemes

Linear schemes use only the information available at the boundary node $\vec{x}_b$ in Eq. (21). That is, they exclude the terms corresponding to the nearest fluid sites $\vec{x}_b - \vec{c}_q$, which is done by setting $\kappa_{-1} = \bar{\kappa}_{-2} = 0$ in Eq. (21). This makes their operation principle local. The disadvantage is that their closure relation only partially satisfies Eq. (12) on arbitrary shaped wall. Their generic closure relation is shown in Eq. (23), according to the derivation performed in Ref. [68]. Based on Eq. (23), it is clear that linear schemes do not support the term accounting for the velocity profile curvature, i.e., the term weighted by α_q^- in Eq. (12). The classical example of the impact of this deficiency is found in Poiseuille flow simulations [46,102,104]. Although the Poiseuille parabolic profile is exactly captured by the LBM in bulk, it fails to be accommodated with the same level of accuracy on boundaries. The corresponding boundary error scales with the square of the grid spacing for no-slip walls, i.e., $\frac{\delta_q^2}{2}\,\partial_q^2 j_q \sim O(\epsilon^2)$, refer to Refs. [48,68,88]. This $O(\epsilon^2)$ scale is denoted in the Error term of Eq. (23). However, this accuracy degrades to first-order when slip is considered. Given that λ scales with H (with Kn fixed), i.e., $\lambda = \mathrm{Kn}/\epsilon \sim O(\epsilon^{-1})$, the neglect of the presence of slip in the accommodation of the profile curvature $\partial_q^2 j_q$ will render the accuracy of the slip boundary scheme formally first-order due to the order of magnitude of the unaccounted term being $\mathcal{C}\,\lambda_q\,\delta_q\,\partial_q^2 j_q \sim O(\epsilon)$. This is denoted in the Error term of Eq. (23):

$$
\begin{aligned}
& j_q(\vec{x}_b) + \alpha_q^+\,\partial_q j_q(\vec{x}_b) + \mathrm{Error} = j_{q\,w}(\vec{x}_w) \\
& \text{with} \quad \mathrm{Error} = \begin{cases} O(\epsilon^2) & \mathrm{no-slip} \\ O(\epsilon) & \mathrm{slip} \end{cases}, \\
& \alpha_q^+ := (\delta_q + \mathcal{C}\,\lambda_q), \\
& \lambda_q := \frac{\lambda}{\Theta_q}, \quad \Theta_q := (\vec{c}_q \cdot \vec{n}), \quad \vec{x}_w = \vec{x}_b + \vec{c}_q\,\delta_q. \qquad (23)
\end{aligned}
$$

The above discussion explains why the previous attempts to implement the slip velocity boundary condition in LBM have shown limitations. Due to their inability to accommodate the velocity curvature, the supported accuracy with respect to the slip boundary condition became restricted to first-order terms in the Taylor series approximation. As a result, in general, only first-order accuracy can be achieved, which is evident from the numerical results shown in previous work, e.g., Refs. [68,69,71]. Still, if the first order accuracy is acceptable, then the class of linear schemes here presented remains appealing, specially due to its local operating principle. The compliance of the boundary scheme with the bulk invariance property of the TRT steady-state solutions is other favorable characteristic supported by the linear schemes here proposed; a feature shared with the parabolic schemes given above. This parametrization attribute is important for consistency purposes. It guarantees that numerical solutions are fixed by the nondimensional groups that control the problem physics, such as Re or Kn.

In terms of implementation, the family of linear schemes is formulated based on the CLI and the MGULI/MGDLI frameworks [47,48]; their parameters are displayed in Table II. Note, they only use α_q^+ as input parameter, which means their closure relation only supports α_q^+ as discussed in the two previous paragraphs and shown in coefficients of Table II. The main difference among these schemes lies in the α_q^+ range of admissibility: (i) $\alpha_q^+ \geqslant 0$ in CLI; (ii) $0 \leqslant \alpha_q^+ \leqslant \frac{1}{2}$ in MGULI; and $\alpha_q^+ \geqslant \frac{1}{2}$ in MGDLI. Once again, we refer to Refs. [46,47,88] for more details on the differences and similarities among them.

C. Kinetic schemes

Kinetic schemes use only the information available at the boundary node $\vec{x}_b$ in Eq. (21). Thus, similarly to linear schemes, they operate locally. The main difference is that: (i) they resort to less information from known populations and (ii) their coefficients do not support any linkwise dependence (although exceptions exist, as discussed at the end of this section). A dedicate analysis to the performance and limitations of these kinetic schemes can be found in Sec. IV of Ref. [68]. Still, it is worth it to reconsider them in this context as they are frequently applied to problems with curved boundaries as well, e.g., Refs. [67,71,82–87].

In the no-slip limit the limitations of the kinetic schemes are well-established as they reduce to the bounce-back rule when $\mathrm{Kn} \to 0$. Because of the midlink boundary location prescribed for each wall cut-link, i.e., $\delta_q = \frac{1}{2}\ \forall$ wall cut-links, the no-slip condition will be necessarily established in a staircase fashion for nonmesh aligned geometries. The impact of this issue on the accuracy of the boundary condition is revealed by the incomplete closure relation displayed in Eq. (24). As shown, only the zeroth-order term in the Taylor series approximation is captured, while the next order term is not supported, meaning kinetic schemes fail to accommodate the velocity profile slope (and obviously the velocity curvature too) at arbitrary wall cut-link distances. In practice, for an arbitrarily located *no-slip* condition, they will introduce a residue of $\delta_q\,\partial_q j_q \sim O(\epsilon)$ in the Taylor series approximation, which explains the first order accuracy in this case. However, in the *slip* case, this accuracy further deteriorates, as revealed by the leading order

residue in the Taylor series approximation which now scales as $\mathcal{C}\,\lambda_q\,\partial_q\,j_q \sim O(1)$, since $\lambda = \mathrm{Kn}/\epsilon \sim O(\epsilon^{-1})$. In general nonmesh aligned configurations the term scaling with λ cannot be fixed. At best, calibrations to correct this term can be made available only for lattice-aligned geometries [46–48,68,88]. Therefore, the leading-order error is indeed $O(1)$, which signifies that kinetic schemes are nothing but zeroth-order accurate approximations to the desired slip velocity condition. That is, kinetic schemes, while first-order accurate towards the no-slip condition, are inconsistent slip models at curved walls. This conclusion is not surprising as any numerical approximation that fails to accommodate the slope of the velocity solution will necessarily fail to represent the slip velocity condition, since the latter requires the capturing of the velocity derivatives on the wall. This rational, previously put forward on theoretical grounds, will be confirmed numerically in Secs. VI and VII.

$$\begin{aligned} & j_q(\vec{x}_\mathrm{b}) + \mathrm{Error} = j_{q\,w}(\vec{x}_\mathrm{w}), \\ & \text{with} \quad \mathrm{Error} = \begin{cases} O(\epsilon) & \mathrm{no-slip} \\ O(1) & \mathrm{slip} \end{cases}, \\ & \vec{x}_\mathrm{w} = \vec{x}_\mathrm{b} + \vec{c}_q\,\delta_q. \end{aligned} \tag{24}$$

In terms of implementation, the family of kinetic schemes may be realized by different formulations. Yet, despite their algorithmic differences, they satisfy the same closure relation as pointed out in Refs. [62,65,68]. For illustrative purposes, here we will consider the diffuse bounce-back (DBB) scheme [55,56,66], whose coefficients are given in Table II. More details on the implementation of the DBB scheme can be found in Refs. [55,68].

Before concluding this section, it is worth commenting on a recent "improvement" proposed by Ref. [67], which attempts to extend the DBB operation principle over curved boundaries. The idea consists in equipping the DBB coefficients with the wall cut-link distance information. Yet, in Ref. [67] those new coefficients are derived for an unidirectional flow along a planar horizontal wall, so that the wall cut-link distance Δ, while variable, takes the same value for all wall cut-links; see Sec. III in Ref. [67] and Appendix B in Ref. [68]. Obviously, this procedure lacks generality in describing curved geometries, where the wall cut-link distances varies link per link; see Fig. 1. To further complicate matters, Ref. [67] extended DBB scheme also leads to a loss of rotational invariance of the LBM bulk solution. It suffices rotating the wall parallel to the diagonal lattice links in a channel flow, a case where an analytical solution is also available as shown in Ref. [68], to confirm that the Ref. [67] strategy is indeed anisotropic. While, in principle, this could be cured by using different calibration coefficients according to the wall orientation, in practice, for nonmesh aligned walls a link per link calibration is not feasible as previously indicated, and further explained in Ref. [68]. Thereby, the Ref. [67] "improved" DBB scheme necessarily introduces angular dependent numerical artefacts; a numerical proof of this defect can be seen in Fig. 9 of Ref. [68]. Besides the accuracy issues previously reported, the "improved" DBB strategy [67] also evidences a rather unstable behavior, since the calibration terms proposed in Ref. [67] often lead to singular coefficients in the boundary scheme algorithm. Other particularly harmful defect refers to the use of viscosity as a calibration parameter in the kinetic boundary algorithms, which inevitably leads to the breakdown of the "viscosity-independent" property of the numerical solutions, even when running on the TRT framework. Because of the aforementioned list of defects, in this study we will limit ourselves to the traditional DBB scheme, e.g., Refs. [55,56,66], which we will take as a representative member of the family of kinetic-based slip schemes with applicability in LBM.

V. STABILITY OF PARABOLIC SLIP SCHEMES

As outlined in Sec. IV, cf. Table II, the input parameters of the parabolic slip schemes are α_q^+ and α_q^-. Thus, in principle, they may take arbitrary positive values. Yet, according to previous heuristic stability recommendations [46], also confirmed in this study, in the boundary update rule, Eq. (21), the coefficients from κ_1 to $\bar{\kappa}_{-2}$ shall remain approximately bounded to $[-1, 1]$. Unfortunately, this may lead to conflicting requirements as frequently the magnitude of α_q^+ and α_q^- grows into much larger values thanks to the slippage contribution. As a result, the MR interpolation coefficients may be pushed outside the aforementioned stability intervals. This kind of instability may therefore restrict the suitability of the LBM slip schemes proposed here to a narrow range of application. In this section a solution to this issue will be presented.

Incidently, we note that [72] also identified their slip LBM boundary schemes to become more unstable than the no-slip ones. Although, in terms of order of accuracy, the Ref. [72] schemes are only roughly comparable to our linear slip schemes. Possibly, it is the over-dissipation caused by their lower order accuracy the reason why the remedy proposed by [72] to improve stability, which is based on relaxation rate limiters, works for them while it is generally insufficient to stabilize our parabolic slip schemes (which evolve according to a higher order operation principle). For that reason, in this section we propose a different and more general strategy, which ensures the stability of our parabolic slip schemes over a broader range of numerical parameters.

Before focusing on the main task of this section, we note that the effect of boundary conditions on the stability of numerical solutions is a rather complicated topic to investigate on a theoretical basis [105]. At best, this task may be attainable under very idealized conditions, as discussed in standard CFD textbooks [106,107]. In the LBM field the study of stability turns out to be even more complex due to the higher number of degrees of freedom available; this aspect of LBM is explained in Chapter 4 of Ref. [41], and apart from a few exceptions, e.g., Ref. [108], the majority of LBM stability studies have been developed on infinitely periodic domains, e.g., Refs. [91,94,109]. Thus, for the purposes of our work, an alternative stability analysis must be pursued, viewing the effect of boundaries.

Here, we have followed a heuristic route to find a way to preserve the stability of the parabolic (MR) slip schemes in the presence of large slippage coefficients. To this end, we have conducted an extensive series of numerical experiments and they all agreed on the conclusion that the instability source, within this problem class, comes from the incoming boundary populations, which are constructed to satisfy the boundary condition for the velocity, but are also employed, via Eq. (5),

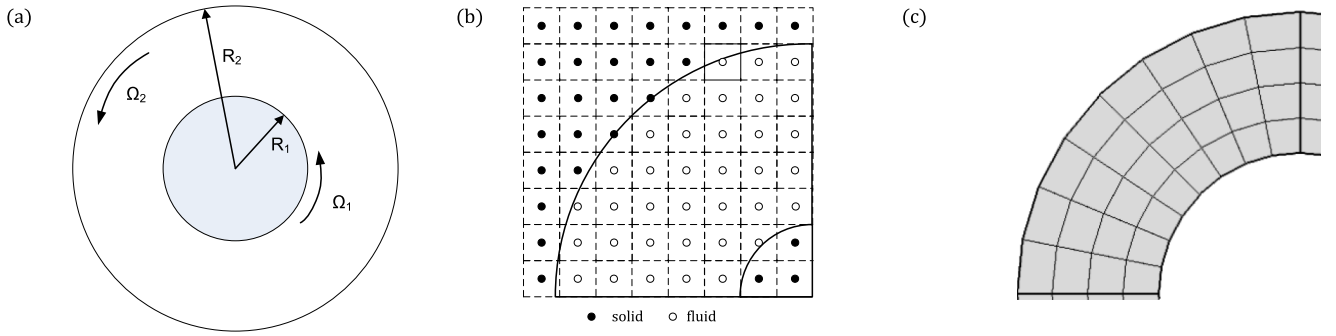

FIG. 2. Cylindrical Couette flow. Panel (a): Problem geometry. Panel (b): LBM discretization. Panel (c): FEM discretization.

to compute the density/pressure at those boundary sites. It is this last feature what will trigger instabilities in our case. Indeed, the problem with the pressure field in reflection-based LBM boundary schemes is not a new issue, and has motivated the development of specific strategies, most notably the non-reflecting boundary conditions, see Chapter 12 in Ref. [41] and references therein. However, these strategies substantially enlarge the complexity of the boundary scheme algorithm. Furthermore, their operation principle fundamentally concerns with the suppression of spurious reflection phenomena that may contaminate the acoustic field. Given that these features go beyond our needs, we opt to follow a simpler route and recompute $\rho(\vec{x}_b)$, at each time step, via extrapolation from bulk. This strategy offers a reliable way to suppress the instability phenomena plaguing the MR slip schemes and, at the same time, is proven to maintain the accuracy of the velocity boundary condition, without adding much complexity to the overall numerical algorithm.

It is well understood from previous LBM works based on extrapolation strategies, e.g., in moving boundary [110] or in mesh refinement problems [111], that the extrapolation of fluid properties, while only affecting a small portion of the computational domain, may have a critical impact on the overall accuracy of the LBM solution. Still, it is recognized [110,111] that a quadratic extrapolation preserves the second-order accuracy of the LBM scheme. Thereby, in this work the reconstruction of the boundary pressure, $P(\vec{x}_b) = c_s^2\,\rho(\vec{x}_b)$, is performed with a quadratic extrapolation scheme, whose formulation is based on Lagragian shape curves, where data points are set along the wall normal direction, according to the procedure explained in Ref. [44]. As this procedure is not new, we refer further details to the above cited literature, e.g., Section 3 of Ref. [44], Table 2 of Ref. [110], or Sections 3 and 4 of Ref. [112]. To differentiate the original parabolic slip schemes [68] from these new ones with enhanced stability characteristics, i.e., subjected to the pressure reconstruction at boundary node $\vec{x}_b$, these latter are marked with a "(⋆)." In Secs. VI and VII we will confirm the good overall stability and accuracy characteristics of the parabolic (⋆) schemes.

VI. NUMERICAL TEST I: CYLINDRICAL COUETTE FLOW IN SLIP-FLOW REGIME

A. Problem formulation and analytical solution

Consider the steady and incompressible viscous motion of a Newtonian fluid caused by the relative rotation of two concentric circular cylinders. The inner and outer cylinders have radii R_1 and R_2 and rotate at angular velocities Ω_1 and Ω_2; see Fig. 2(a). This setup is representative of gas lubrication applications, where the interest in the slip-flow regime has been gaining particular relevance, see Refs. [74–76]. In this flow the inertial terms are nonzero and are exactly balanced by the radial pressure. As for the circumferential component, the general solution of the velocity profile is given by

$$u_\theta(r) = \frac{a}{r} + b\,r, \tag{25}$$

with $R_1 \leqslant r \leqslant R_2$. At the inner and outer cylinder surfaces the slip boundary conditions hold:

$$u_\theta(R_1) = \Omega_1\,R_1 + \mathcal{C}_1\,\lambda\left(\frac{\partial u_\theta}{\partial r} - \frac{u_\theta}{r}\right)\bigg|_{r=R_1}, \tag{26a}$$

$$u_\theta(R_2) = \Omega_2\,R_2 - \mathcal{C}_2\,\lambda\left(\frac{\partial u_\theta}{\partial r} - \frac{u_\theta}{r}\right)\bigg|_{r=R_2}. \tag{26b}$$

By solving Eq. (25) subjected to Eqs. (27), the integration constants a and b are obtained:

$$a = -\frac{R_1^3\,R_2^3\,(\Omega_2 - \Omega_1)}{R_1\,R_2\left(R_2^2 - R_1^2\right) + 2\,\lambda\left(\mathcal{C}_2\,R_1^3 + \mathcal{C}_1\,R_2^3\right)}, \tag{27a}$$

$$b = \frac{R_1\,R_2\left(R_2^2\,\Omega_2 - R_1^2\,\Omega_1\right) + 2\,\lambda\left(\mathcal{C}_2\,R_1^3\,\Omega_1 + \mathcal{C}_1\,R_2^3\,\Omega_2\right)}{R_1\,R_2\left(R_2^2 - R_1^2\right) + 2\,\lambda\left(\mathcal{C}_2\,R_1^3 + \mathcal{C}_1\,R_2^3\right)}. \tag{27b}$$

Figure 3 illustrates typical velocity profiles of the cylindrical Couette flow solution, given by Eq. (25) with Eqs. (27). Two

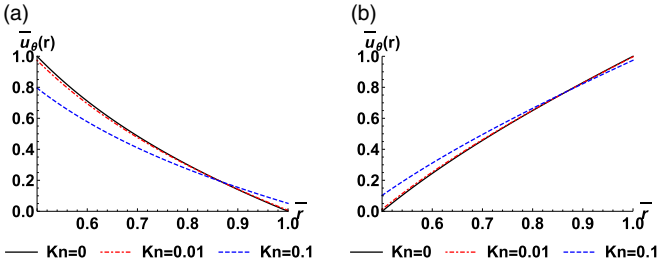

FIG. 3. Cylindrical Couette flow velocity profiles as function of $\mathrm{Kn} = \frac{\lambda}{R_2 - R_1}$, for $R_1/R_2 = 1/2$, $\mathcal{C}_1 = \mathcal{C}_2 = 1$. Panel (a): $\Omega_1 = 0.001$ and $\Omega_2 = 0$ ($\bar{u}_\theta = u_\theta/(\Omega_1\,R_1)$ and $\bar{r} = r/R_2$). Panel (b): $\Omega_1 = 0$ and $\Omega_2 = 0.001$ ($\bar{u}_\theta = u_\theta/(\Omega_2\,R_2)$ and $\bar{r} = r/R_2$).

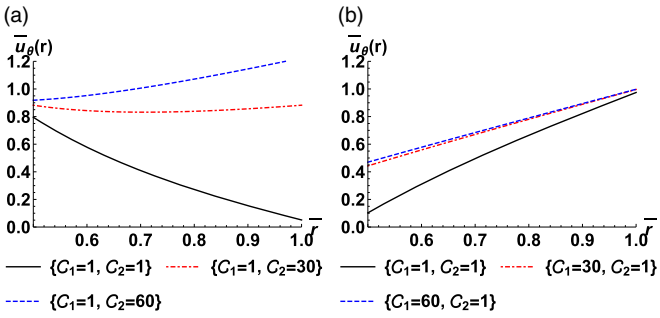

FIG. 4. Cylindrical Couette flow velocity profiles as function of $\{\mathcal{C}_1, \mathcal{C}_2\}$, for $R_1/R_2 = 1/2$ and $\mathrm{Kn} = \frac{\lambda}{R_2 - R_1} = 0.1$. Panel (a): $\Omega_1 = 0.001$ and $\Omega_2 = 0$ ($\bar{u}_\theta = u_\theta/(\Omega_1 R_1)$ and $\bar{r} = r/R_2$). Panel (b): $\Omega_1 = 0$ and $\Omega_2 = 0.001$ ($\bar{u}_\theta = u_\theta/(\Omega_2 R_2)$ and $\bar{r} = r/R_2$).

TABLE III. Specification of the boundary schemes used in this numerical test. Each boundary class groups boundary schemes of identical order of accuracy, according to the description given in Sections IV A, IV C, and IV B; the theoretical order of accuracy of the FEM [Linear] and FEM [Parabolic] is second- and third-order [107,114], respectively. This table summarizes the specific boundary schemes, i.e., algorithms, pertaining to each class.

Boundary class	Specific boundary scheme
Kinetic	Diffuse bounce-back scheme (DBB)
Linear	Central linear scheme (CLI)
Parabolic	Multireflection scheme (MR1)
Parabolic ($\star$)	Multireflection scheme (MR1) with pressure reconstruction
FEM [Linear]	Linear shape functions
FEM [Parabolic]	Quadratic shape functions

cases are considered: (a) inner cylinder rotates and outer cylinder is at rest; and (b) inner cylinder is at rest and outer cylinder rotates. It is well-established [113] that the influence of the geometry curvature on slip may differ significantly over concave and convex surfaces. In this sense the cylindrical Couette flow is particularly revelent as it contains both concave and convex surface shapes. The characteristic geometrical parameter defining this problem is given by the ratio R_1/R_2. Without loss of generality, we will fix it to $R_1/R_2 = 1/2$. The fundamental nondimensional group governing this problem is the Knudsen number. We define it as $\mathrm{Kn} = \frac{\lambda}{H}$, where $H := (R_2 - R_1)$.

As shown in Fig. 3, at $\mathrm{Kn} = 0.01$ the slippage effect is nearly negligible, and the velocity profile approximately matches the no-slip case $\mathrm{Kn} = 0$, except close to walls (particularly the convex one). However, at $\mathrm{Kn} = 0.1$ the slip phenomenon becomes noticeable everywhere.

Besides the Knudsen number, the other important parameter determining the shape of velocity profiles refers to the slip coefficients. Under certain slippage conditions, the rotating case $\Omega_1 \neq 0$ and $\Omega_2 = 0$ may lead to a nonintuitive phenomenon called velocity inversion [74–76]. Following [76], the necessary condition for the velocity profile to become inverted is $\mathcal{C}_2 > \frac{R_2}{\lambda}$, whereas the stronger requirement for the full velocity profile to be inverted is $\mathcal{C}_2 > \frac{R_2}{2\lambda}[1 + (\frac{R_2}{R_1})^2]$; both conditions hold $\forall\ \mathcal{C}_1$. In the opposite rotating case, i.e., when $\Omega_1 = 0$ and $\Omega_2 \neq 0$, the conventional velocity profile is always recovered, meaning no velocity inversion can possibly occur $\forall\ \{\mathcal{C}_1, \mathcal{C}_2\}$ [76]. Figure 4 illustrates these two rotation scenarios, considering $R_2/R_1 = 1/2$ and $\mathrm{Kn} = 0.1$ (with $\lambda = 0.05$). When $\Omega_1 \neq 0$ and $\Omega_2 = 0$, three different profiles are possible: (i) conventional at $\mathcal{C}_2 = 1$, (ii) partially inverted at $\mathcal{C}_2 = 30$, and (iii) fully inverted at $\mathcal{C}_2 = 60$. We note that the case of large slippage coefficients is representative of walls where specular reflection dominates over diffuse reflected particles [9,12], i.e., $\sigma_v \to 0$ as displayed in Table I. The other rotating case $\Omega_1 = 0$ and $\Omega_2 \neq 0$ always feature conventional velocity evolutions $\forall\ \{\mathcal{C}_1, \mathcal{C}_2\}$. All cases discussed here will be numerically studied below.

The accuracy of the numerical solutions u_θ, is measured with respect to the analytical solution, $u_\theta^{(\mathrm{exact})}$, given by Eq. (25) with Eqs. (27). Here, the error measure is computed as

$$|\mathcal{E}_u| = \sqrt{\frac{\sum \left(u_\theta - u_\theta^{(\mathrm{exact})}\right)^2}{\sum \left(u_\theta^{(\mathrm{exact})}\right)^2}}, \tag{28}$$

where sums are taken over all grid points.

B. Numerical implementation

For the numerical study, we investigate the accuracy of LBM and FEM in simulating the cylindrical Couette flow along three fluid-wall interaction regimes: (i) no-slip $\mathrm{Kn} = 0$, (ii) moderate slip $\mathrm{Kn} = 0.01$, and (iii) large slip $\mathrm{Kn} = 0.1$. We adopt the standard LBM-TRT technique, which operates on a uniform Cartesian mesh (built on the d2Q9 lattice model), and we examine three groups of boundary schemes: (a) kinetic schemes (modeled with DBB rule [55,67,68,85]), (b) linear schemes (modeled with CLI slip scheme [47,48,68]), and (c) parabolic schemes (modeled with MR1 slip scheme [46,47,68]); this information is compiled in Table III with mathematical details found in Table II. FEM operates on rectangular elements, structured on a body-fitted mesh [73], see Fig. 2(c), where we follow the isoparametric formulation [107,114] using: (a) linear elements (denoted as linear FEM), and (b) quadratic elements (denoted as parabolic FEM); their theoretical order of accuracy is, respectively, second- and third-order [107,114]. Figures 2(b) and 2(c) illustrate the geometry discretization using LBM and FEM, respectively. In both LBM and FEM, simulations are initialized for a rest state $\vec{u} = \vec{0}$ and an uniform pressure field $P = 1/3$ (in numerical units). In LBM the populations are initialized to their equilibrium state. The steady-state is assumed to be reached: (i) in LBM for the magnitude of the relative difference in velocity $|u_\theta(t)/u_\theta(t - t_a) - 1| < 10^{-10}$, with $t_a = 10^2$ simulation time steps; (ii) in FEM for the magnitude of the relative residual smaller than 10^{-10} in the GMRES iterative solver of COMSOL software [73]. The numerical study focuses on the following three points: (i) the effect of grid resolution; (ii) the effect of TRT relaxation parameter Λ; and (iii) the effect of slippage coefficients.

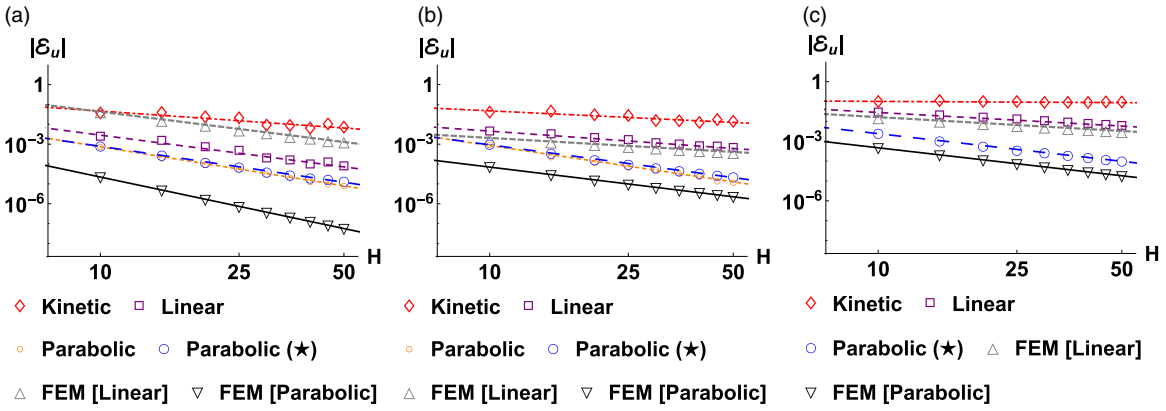

FIG. 5. Cylindrical Couette flow with $\Omega_1 = 0.001$ and $\Omega_2 = 0$. Accuracy $|\mathcal{E}_u|$ as function of grid resolution H (note, $H := R_2 - R_1$), where $R_1/R_2 = 1/2$ and $\Lambda = 3/16$ are fixed. Convergence rates are quantified in Table IV. Panel (a): No-slip flow regime (Kn $= 0$). Panel (b): Moderate slip-flow regime (Kn $= 0.01$, $\mathcal{C}_1 = \mathcal{C}_2 = 1$). Panel (c): Large slip-flow regime (Kn $= 0.1$, $\mathcal{C}_1 = \mathcal{C}_2 = 1$).

1. Effect of grid resolution

Figures 5 and 6 present mesh refinement tests for the different numerical schemes considered in this work. Their convergent rates are quantified in Tables IV and V, respectively. These numerical outcomes refer to the simulation of the velocity plots shown in Fig. 3. Next, we will discuss each case individually.

The first case, Kn $= 0$, corresponds to the modeling of no-slip walls. As expected, kinetic schemes reduce to the bounce-back rule in this case. Thus, only first-order accuracy is supported. Linear schemes are second-order accurate with respect to the no-slip condition. Parabolic schemes improve this accuracy to almost third-order, and further reduce the overall error magnitude. Linear FEM, which operates on linear elements, also supports the second-order accuracy, but it tends to produce larger errors than LBM with boundary schemes of identical order of accuracy. The reason has been identified in previous works, e.g., Refs. [115,116], and it lies on how each numerical scheme handles the boundary condition. In LBM the boundary condition is established implicitly, through a Taylor series approximation, which permits a smooth accommodation of the velocity profile on the wall (although at costs of a truncation error in the boundary condition prescription due to the finite Taylor series approximation). Differently, FEM explicitly enforces the boundary condition to be exact at the boundary nodes. Yet, when the bulk solution is not sufficiently accurate, rather than beneficial, the constraint to exactly satisfy the boundary condition may lead to the distortion of the velocity profile in the attempt to accommodate it. This explains the smaller errors of the LBM linear schemes compared to linear FEM, although both are formally second-order accurate. Obviously, this weakness can be improved with the use of more accurate discretizations in FEM. For instance, parabolic FEM, which employs quadratic elements, provides a better fit of the velocity solution. This improvement is reflected in smaller numerical errors and close to fourth-order convergence rate in the numerical accuracy. The price to pay is the substantial increase in the complexity and computational cost of the algorithm; while linear elements (linear FEM) lead to a triadiagonal system, the system to solve with quadratic elements (parabolic FEM) is pentadiagonal [107].

The second case, Kn $= 0.01$, considers a small slip magnitude, so that the no-slip profile is almost replicated. This scenario permits verifying the previous discussion on the source of inaccuracy of linear FEM solutions being caused by the stiffer profile accommodation. Here, due to the prescription of slip on the boundary condition, the degree of constraint gets weakened. Therefore, for a velocity profile alike the no-slip

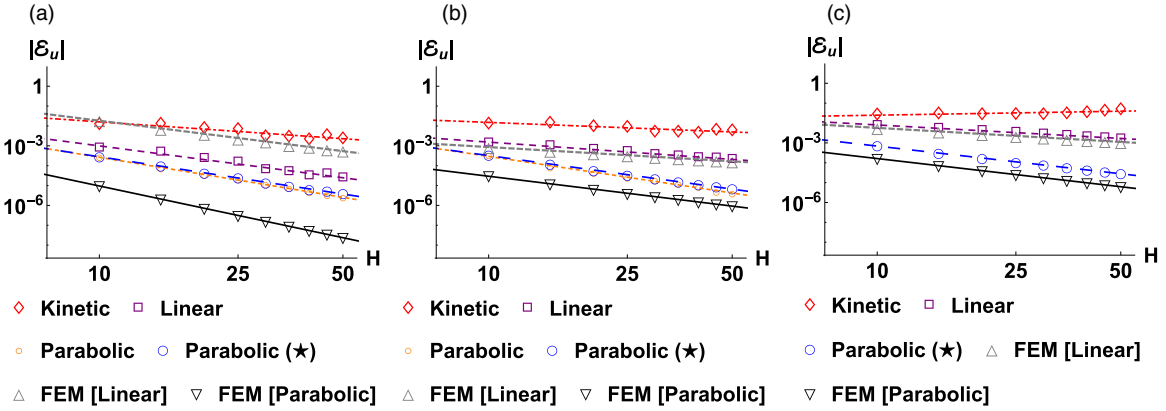

FIG. 6. Same as Fig. 5, but with $\Omega_1 = 0$ and $\Omega_2 = 0.001$. Panel (a): No-slip flow regime (Kn $= 0$). Panel (b): Moderate slip-flow regime (Kn $= 0.01$, $\mathcal{C}_1 = \mathcal{C}_2 = 1$). Panel (c): Large slip-flow regime (Kn $= 0.1$, $\mathcal{C}_1 = \mathcal{C}_2 = 1$).

TABLE IV. Quantification of convergence rates in Fig. 5, obtained through linear regression.

	Convergence rates		
Numerical schemes	(a) Kn = 0	(b) Kn = 0.01	(c) Kn = 0.1
Kinetic scheme	−1.22	−0.83	−0.09
Linear scheme	−2.28	−1.25	−0.98
Parabolic scheme	−2.81	−2.61	Unstable
Parabolic (⋆) scheme	−2.59	−2.36	−1.99
FEM [Linear]	−2.18	−1.01	−0.99
FEM [Parabolic]	−3.71	−2.14	−2.01

TABLE V. Quantification of convergence rates in Fig. 6, obtained through linear regression.

	Convergence rates		
Numerical schemes	(a) Kn = 0	(b) Kn = 0.01	(c) Kn = 0.1
Kinetic scheme	−1.21	−0.69	0.29
Linear scheme	−2.29	−1.25	−0.97
Parabolic scheme	−2.88	−2.64	Unstable
Parabolic (⋆) scheme	−2.68	−2.42	−1.99
FEM [Linear]	−2.19	−1.02	−1.01
FEM [Parabolic]	−3.72	−2.15	−2.03

case, much smaller numerical errors can be recovered with linear FEM, as visible in Figs. 5(b) and 6(b). Yet, the convergence rate is inevitably degraded to the first order. Similar conclusions on the order of convergence are obtained with the LBM equipped with linear slip schemes, which comply with the theoretical analysis conducted in Sec. IV; see Eq. (23). However, LBM equipped with parabolic slip schemes support the same accuracy characteristics of the no-slip condition, further competing with the accuracy of the parabolic FEM, which is formally higher-order accurate.

The third and final case, Kn = 0.1, addresses the large slip regime. Here, the global velocity solution gets dominated by the gas-surface interactions. Therefore, the modeling of the slip condition plays the dominating role on the accuracy of the numerical simulations. Consequently, this large Kn test provides an unambiguous validation exercise to the theoretical analysis developed in Sec. IV, concerning the accuracy of the LBM slip boundary schemes in the slip regime. As expected, kinetic schemes (whatever calibration is used) are zeroth-order accurate, and therefore inconsistent as slip velocity boundary models. Slightly better performance is achieved by linear slip schemes, which are bounded to first-order accuracy, the same accuracy reproduced by the linear FEM in the slip-flow regime. Parabolic slip schemes reach the highest exactness. Yet, traditional parabolic schemes may also become unstable at large Kn due to the large slippage contribution which may largely increase the magnitude of the MR coefficients, recall discussion in Sec. V. Nonetheless, stability can be guaranteed with the procedure suggested in Sec. V, whose schemes are denoted by parabolic (⋆). They support the same level of accuracy of traditional parabolic schemes in a stable manner, and their accuracy even matches that of parabolic FEM with slip boundary conditions, which are formally of higher-order accuracy.

The ensemble of numerical tests reported here attests the superiority of the LBM parabolic schemes, from no-slip to large slip regimes. Most notably, this advantage tends to be more significant in the slip-dominated regimes. In fact, the second-order accuracy of the LBM becomes even comparable to FEM adopting formally higher-order accurate discretizations performed over state-of-the-art body-fitted meshes. For that reason, due to the ease of implementation offered by the LBM uniform mesh discretization combined with the superb level of accuracy here demonstrated, it can be stated that LBM is indeed an appealing route to simulate geometrically nontrivial flows pertaining to the slip-flow regime.

2. *Effect of TRT relaxation parameter* Λ

The accuracy of LBM solutions can be further improved by exploring the additional collision degree of freedom Λ, which comes available with the TRT scheme. We recall that Λ expresses the product of symmetric Λ^+ and antisymmetric Λ^- eigenfunctions, where the former is determined by viscosity while the latter is free to adjust. Figures 7 and 8 illustrate the impact of Λ on the accuracy of the solutions presented in Figs. 5 and 6, respectively. We restrict this study to a

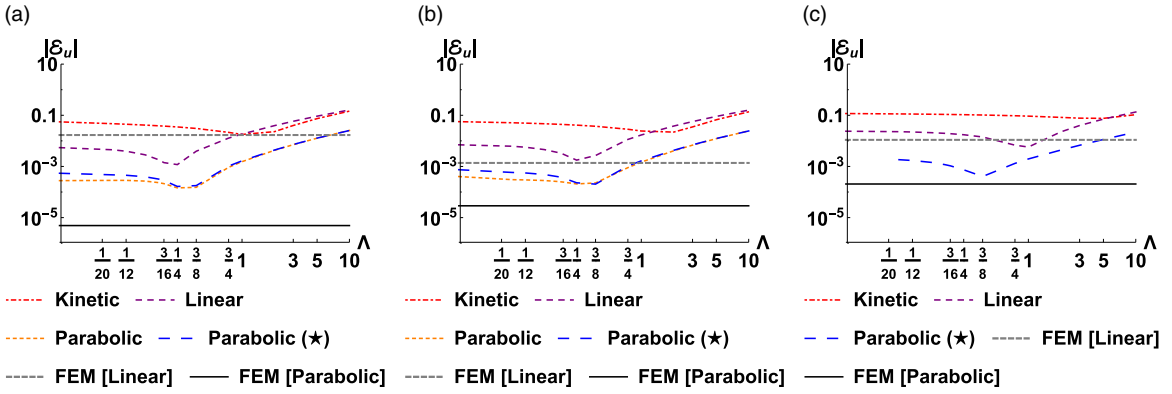

FIG. 7. Cylindrical Couette flow with $\Omega_1 = 0.001$ and $\Omega_2 = 0$. Accuracy $|\mathcal{E}_u|$ as function of Λ, with $H = 15$ fixed (note, $H := R_2 - R_1$) and $R_1/R_2 = 1/2$. Panel (a): No-slip flow regime (Kn = 0). Panel (b): Moderate slip-flow regime (Kn = 0.01, $\mathcal{C}_1 = \mathcal{C}_2 = 1$). Panel (c): Large slip-flow regime (Kn = 0.1, $\mathcal{C}_1 = \mathcal{C}_2 = 1$).

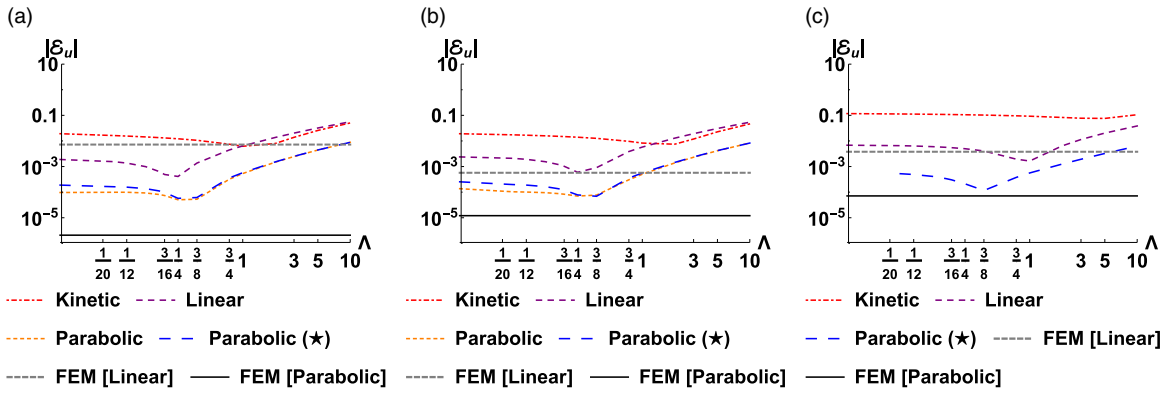

FIG. 8. Same as Fig. 7 but with $\Omega_1 = 0$ and $\Omega_2 = 0.001$. Panel (a): No-slip flow regime (Kn $= 0$). Panel (b): Moderate slip-flow regime (Kn $= 0.01$, $\mathcal{C}_1 = \mathcal{C}_2 = 1$). Panel (c): Large slip-flow regime (Kn $= 0.1$, $\mathcal{C}_1 = \mathcal{C}_2 = 1$).

coarse mesh scenario, where the flow is resolved by $H = 15$ computational cells along the cylinders gap ($H := R_2 - R_1$). Numerical evidence indicates that conclusions remain qualitatively equivalent on finer meshes. The comparison of Fig. 7 against Fig. 8 suggests that the Λ effect on accuracy is qualitatively identical whether we have $\{\Omega_1 = 0, \Omega_2 \neq 0\}$ or $\{\Omega_1 \neq 0, \Omega_2 = 0\}$. The main difference is quantitative and refers to the order of magnitude of the error, generally smaller when $\{\Omega_1 = 0, \Omega_2 \neq 0\}$. For LBM users, the main interest of this study lies in the provision of guidelines on the optimal Λ choice; i.e., the Λ value which makes $|\mathcal{E}_u|$ minimum. In principle, the best Λ choice is expected to vary with the physical regime, owing to the associated variations that the flow features undergo. In the process of capturing them, the order of accuracy of the boundary scheme is also expected to impact the influence of Λ on the solution. This test reveals that, for the low-order slip schemes (i.e., kinetic and linear schemes) the optimal Λ is shifted toward larger values when Kn increases, while with parabolic schemes the optimal Λ remains fixed, around $\Lambda = 3/8$. From the above exposed, the value $\Lambda = 3/8$ is recommended as a good starting point to tackle this kind of flow, where solution evolves according to circular streamlines.

3. Effect of slippage coefficients

Finally, the study shown in Fig. 9 illustrates how the accuracy of the numerical schemes is affected by the magnitude of the slippage coefficients. Here, we keep the same simulation

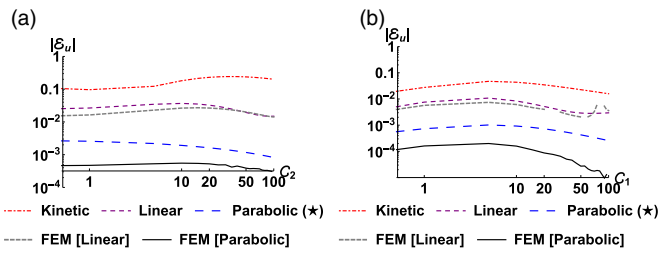

FIG. 9. Cylindrical Couette flow accuracy $|\mathcal{E}_u|$ at Kn $= 0.1$ as function of slippage coefficients, with $\Lambda = 3/16$, $H = 15$ (note, $H := R_2 - R_1$), and $R_1/R_2 = 1/2$ fixed. Panel (a): $\Omega_1 = 0.001$ and $\Omega_2 = 0$ with $\mathcal{C}_1 = 1$ and $\mathcal{C}_2 \in [0, 100]$. Panel (b): $\Omega_1 = 0$ and $\Omega_2 = 0.001$ with $\mathcal{C}_1 \in [0, 100]$ and $\mathcal{C}_2 = 1$.

parameters used before in the Λ study. Figure 9(a) addresses the case where the velocity solutions experience the more drastic changes, namely: a normal profile at $\mathcal{C}_2 \in [0, 20[$, a partially inverted profile at $\mathcal{C}_2 \in [20, 50[$, and a fully inverted profile at $\mathcal{C}_2 \in [50, \infty[$. Despite these profile differences, we note that the more regular case, given by Fig. 9(b) where the velocity profile holds invariant characteristics $\forall \mathcal{C}_1$, displays a qualitatively similar error behavior. In general, the maximum error magnitude is reached at intermediate slip values. This corresponds to the case where the interplay between bulk and boundary undergoes a more delicate balance, and as such it becomes more sensitive to the numerical scheme accuracy.

VII. NUMERICAL TEST II: PERMEABILITY ACROSS PERIODIC ARRAY OF CIRCULAR CYLINDERS IN SLIP-FLOW REGIME

A. Problem formulation and reference solution

Consider the steady and incompressible viscous motion of a Newtonian fluid across a square periodic array of solid circular cylindrical obstacles. This setup is a typical benchmark in the validation of computer models in porous media, where the interest in the slip-flow regime has been gaining particular relevance, e.g., Refs. [78–82]. The geometry of this problem is illustrated in Fig. 10(a). The fluid motion is assumed to develop in the linear (creeping flow) regime, i.e., inertial effects are excluded in the hydrodynamic equations. Depending on the Kn regime, the cylinders surfaces are subjected to either the no-slip or the slip conditions. In this latter case, the complexity of this test is intensified by the breakdown of the constant slip condition, meaning $\frac{\partial j_\theta}{\partial \theta} = 0$ no longer holds, which was a requirement invoked during the formulation of our slip boundary schemes, recall Sec. III. The relevant governing parameters controlling this problem are: (i) the Knudsen number, defined as Kn $:= \frac{\lambda}{R}$, (ii) the slippage coefficient $\mathcal{C}$ at the surface of the solid obstacles, and (iii) the concentration of the cylinders embedded in the flow environment, defined as $p := \frac{\pi R^2}{H^2}$, see Fig. 10(a). In this work we will focus on the case of dilute solid volume fractions, i.e., $p \ll 1$, and, without loss of generality, take $p = 0.2$ for the rest of this study, as followed in previous studies [46,116,117].

While this problem is not accessible to exact closed-form solutions for the local velocity and pressure fields, the

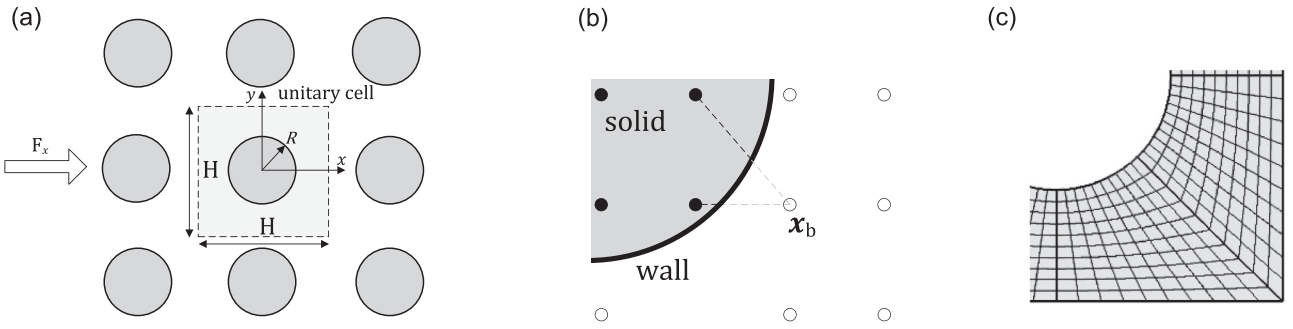

FIG. 10. Periodic array of solid cylindrical obstacles. Panel (a): Problem geometry. Panel (b): LBM discretization. Panel (c): FEM discretization.

computation of the global permeability of the system k_{eff} is available via semi-analytical methods. In the no-slip case, i.e., $\text{Kn} = 0$, we use the reference permeability solutions, $k_{\text{eff}}^{(\text{ref})}$, presented in Table VI of Ref. [46]. The slip case often uses, as semi-analytical method, the cell model [118–120] to determine the reference permeability solutions, e.g., Refs. [71,85,87]. Yet, as explained in Appendix B, they tend to be not sufficiently accurate for benchmark purposes. For that reason, in the slip-flow regime, we adopt as reference solution, $k_{\text{eff}}^{(\text{ref})}$, the outcome of FEM simulations run on extremely fine meshes (using up to 400 grid nodes along the half gap distance in between adjacent cylinders), with P3/P2 elements in the discretization of the velocity/pressure solution. Giving the reference permeability, $k_{\text{eff}}^{(\text{ref})}$, we measure the accuracy of the numerical solutions as

$$\left|\mathcal{E}_{k_{\text{eff}}}\right| = \left|\frac{k_{\text{eff}}}{k_{\text{eff}}^{(\text{ref})}} - 1\right|, \quad k_{\text{eff}} = \frac{\nu\,\langle j_x\rangle}{F_x}. \tag{29}$$

Note, the fluid viscosity ν and the external body force F_x are input parameters. The volume averaged momentum $\langle j_x\rangle$ corresponds to the outcome of numerical solutions [46,92]. That is, $\langle j_x\rangle$ is obtained as a post-processing quantity through numerical quadratures; specifically, the mid-point rule in LBM and the "trapezoidal" rule in FEM. While we acknowledge numerical integration errors are introduced, see Refs. [92,116,117], this error source becomes unimportant in this study since we are interested in relative differences between schemes, i.e., its effect cancels out.

B. Numerical implementation

Due to the periodic arrangement of this problem, the geometry simulated is reduced to one unitary cell with periodic boundary conditions all over; see Fig. 10(a). The flow is generated by an applied body force F_x and the steady-state criterion is determined by $|k_{\text{eff}}(t)/k_{\text{eff}}(t-t_a) - 1| < 10^{-10}$, with $t_a = 10^2$ simulation time steps. As in Sec. VI, the LBM discretization is performed on the d2Q9 uniform mesh, see Fig. 10(b), while the FEM discretization adopts a high quality body-fitted structured mesh, as shown in Fig. 10(c). Again, the following LBM boundary schemes are considered: (a) kinetic schemes (modeled with DBB rule [55,67,68,85]), (b) linear schemes (modeled with CLI slip scheme [47,48,68]), and (c) parabolic schemes (modeled with MR1 slip scheme [46,47,68]); see Table VI for a summary and Table II for the mathematical details. Once again, we consider two types of parabolic schemes: the standard ones (simply denoted as parabolic) and those with enhanced stability [denoted as parabolic (⋆)]. However, due to the particular nature of this flow problem, we observed that the single use of parabolic (⋆) schemes, while notably improving stability, might compromise the accuracy of solutions. Therefore, we apply an hybrid strategy, called *mix parabolic (⋆)*. According to this implementation, boundary nodes located close to the cylinder stagnation region operate with the parabolic (⋆) strategy, while the remaining ones continue to run with the standard parabolic scheme. We find that this mixed-type strategy preserves both stability and accuracy. The rest of the numerical implementation follows the steps explained in Sec. VI. As before, we examine the accuracy of the boundary schemes with respect to two fluid-wall interaction regimes: (a) no-slip $\text{Kn} = 0$, and (b) large slip $\text{Kn} = 0.1$. In both situations we will evaluate the following numerical aspects: (i) the effect of TRT relaxation parameter Λ; and (ii) the effect of slippage coefficients $\mathcal{C}$.

1. *Effect of TRT relaxation parameter* Λ

It is worth reassessing the effect of Λ on the solution accuracy, since the present test displays a different flow structure compared to the cylindrical Couette flow case, i.e., now there are stagnation streamlines. With this study, we aim at identifying general qualitative features of the free-parameter Λ, given by $\Lambda = \Lambda^+\Lambda^-$, and its impacts on the permeability solutions in no-slip and slip-flow regimes. Here, we limit the

TABLE VI. Summary of the boundary schemes used in this numerical test. More details given in caption of Table III.

Boundary class	Specific boundary scheme
Kinetic	Diffuse bounce-back scheme (DBB)
Linear	Central linear scheme (CLI)
Parabolic	Multireflection scheme (MR1)
Mix Parabolic (⋆)	Multireflection scheme (MR1) mixing standard scheme with pressure reconstruction one
FEM [Linear]	Linear shape functions
FEM [Parabolic]	Quadratic shape functions

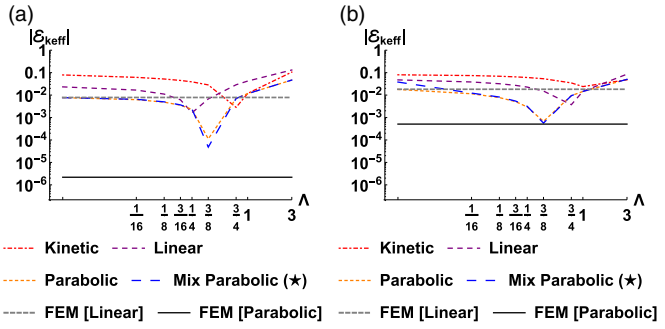

FIG. 11. Permeability of a creeping flow across a periodic array of cylindrical obstacles at low volume fraction $p = 0.2$. Accuracy $|\mathcal{E}_{k_{\text{eff}}}|$ as function of Λ, with $H = 33$ fixed [H is defined on Fig. 10(a)]. Panel (a): No-slip flow regime (Kn $= 0$). Panel (b): Large slip-flow regime [Kn $= 0.1$, $\mathcal{C} = 1$)].

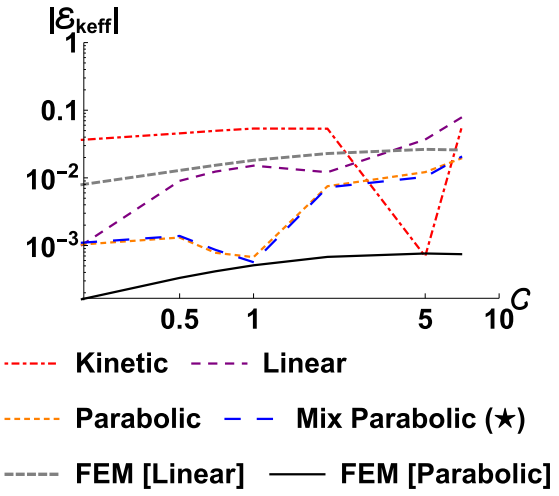

FIG. 12. Permeability of a creeping flow across a periodic array of cylindrical obstacles at low volume fraction $p = 0.2$, developing in large slip-flow regime (Kn $= 0.1$). Accuracy $|\mathcal{E}_{k_{\text{eff}}}|$ as function of slippage coefficient $\mathcal{C}$, with $\Lambda = 3/16$ and $H = 33$ fixed [H is defined on Fig. 10(a)].

subsequent discussion to coarse grid resolutions. (Although, we have numerical evidence that, at finer grids, the trends reported here are very much alike.)

Figure 11 presents the results of this test in both no-slip and slip-flow regimes. Despite the differences in the flow solution, the comparison of Fig. 11 against Figs. 7 and 8 reveals that the effect of Λ on accuracy holds approximately unchanged. As before, the optimal Λ choice increases with Kn for low order slip schemes, such as kinetic and linear schemes. Particularly, for linear schemes the minimum in $|\mathcal{E}_{k_{\text{eff}}}|$ usually swipes the interval $\Lambda \in [1/4, 3/4]$. However, for parabolic schemes the minimum in $|\mathcal{E}_{k_{\text{eff}}}|$ holds constant and fixed around $\Lambda \approx 3/8$, regardless the Kn regime. This conclusion is consistent with that in Sec. VI. Another general conclusion, also in agreement with Sec. VI, refers to the exceptional performance of parabolic slip schemes compared to linear FEM, and even parabolic FEM. Overall, the accuracy of parabolic slip schemes, operating in the range $\Lambda \lesssim 3/4$, always supersedes that of linear FEM. This observation holds for all Kn regimes tested. In the slip-flow regime, the parabolic slip schemes operating at $\Lambda = 3/8$ even reach the level of accuracy of parabolic FEM (which is formally third-order accurate). The reason why the numerical error of the LBM parabolic schemes in these problem tests is consistently minimized around $\Lambda = 3/8$ holds unclear. Based on the small order of magnitude of the numerical error, the answer to this question is expected to be subtle. Namely, to depend on the interplay between bulk and boundary numerical errors, rather than on a single numerical source alone. Yet, before a proper theoretical explanation can be devised, we believe that additional numerical support is required.

In conclusion, this numerical test and the one reported in Sec. VI confirm the competitiveness of LBM as a CFD tool where, compared to FEM, the use of LBM appears particularly interesting in the slip-dominated regimes.

2. Effect of slippage coefficients

In this section we investigate the impact of the slippage magnitude on the accuracy of the numerical schemes. The clarification of this issue is important as this problem does not exactly comply with the constant slip condition $\frac{\partial j_\theta}{\partial \theta} = 0$, which was invoked during the derivation of our slip schemes.

Figure 12 illustrates this study, employing $H = 33$ computational cells, i.e., the same mesh size adopted before, and $\Lambda = 3/16$. The accuracy values here observed follow those identified in Figs. 9(a) and 9(b) of Sec. VI. Namely, the accuracy of parabolic slip schemes lies somewhere in between linear FEM and parabolic FEM. However, taking as reference Sec. VI, all numerical schemes here experience a clear loss of accuracy (and also stability) with the increase of the slippage magnitude. This negative feature may be explained by three reasons. First, due to the existence of stagnation regions on the cylindrical wall surface, the solution may be more prone to instabilities with origin on the wall pressure, recall discussion in Sec. V. Second, because the limit $\mathcal{C} \gg 1$ produces a change in the mathematical nature of the boundary condition, i.e., the slip velocity condition may tend to shift over a free-slip condition. Consequently, the LBM modeling of the free-slip requests a different type of linkwise boundary scheme, e.g., based on the specular reflection operation principle [47]. Third and final, because $\frac{\partial j_\theta}{\partial \theta} = 0$ is not exactly fulfilled in this test, convergence towards this condition may be impaired. In spite of that, the incompatibility with this last constraint may be mitigated, e.g., by smoothing $\frac{\partial j_\theta}{\partial \theta}$ variations through mesh refinement.

VIII. CONCLUSIONS

This work investigates the application of the lattice Boltzmann method (LBM) as a competent computional fluid dynamics (CFD) tool to simulate gaseous isothermal flows in the slip-flow regime. This demands the existence of consistent LBM boundary schemes for the slip velocity boundary condition, applicable at arbitrary curved walls. The goal is that slip and no-slip boundary conditions can be used on an equal footing in numerical implementations. However, this task is

not straightforward for a number of reasons. First, compared to the no-slip case, which imposes a Dirichlet (specified value) boundary condition, the slip velocity condition is a Robin-type boundary condition, defined as a mix of Dirichlet and Neumann (specified gradient) boundary conditions. Second, this mixed character may lead to a compatibility problem between the numerical approximation of bulk and boundary derivatives. Third, and related to this second point, is that the boundary derivative is often implemented on discrete operators with asymmetrical stencils, which for the same accuracy demand a larger number of grid points and may damage stability too. Fourth and final, the explicit form of these terms is surface shape dependent, which means wall tangent and normal directions must be locally determined to faithfully reproduce the wall curvature (concave/convex) effects. Given all these difficulties, this work has proposed exploring the LBM particular characteristics to operate with a more favorable numerical strategy.

Contrary to common practice, in this work we have not searched for a relationship between LBM and kinetic theory boundary conditions. Rather, we have made explicit use of the working principle of typical LBM boundary schemes, i.e., based on reflection-type rules, and worked out the form of their closure relations to approximate the intended physical slip velocity condition, as given by Eq. (1). This task was motivated by the fact that both frameworks evolve according to a truncated Taylor series of the fluid velocity at the boundary. Although this result was already given in Ref. [68], only planar walls were addressed. In this paper we extend this result to arbitrary curved surfaces, which is not trivial since, with the addition of the surface curvature, the physical model to take into account is given by a different relation. Namely, for plane walls the slip condition is only dictated by the velocity derivative normal to the wall, while for curved walls the full shear stress tensor must be considered. Only the inclusion of the stress tensor leads to the appearance of surface curvature corrections in the wall slip model, which are fundamental to correctly capture slippage phenomena specific of nonplanar surfaces, such as the velocity inversion phenomenon in a cylindrical Couette flow [76,77].

To evaluate the ability of the LBM slip boundary schemes considered herein, our procedure includes the following three steps. First, we theoretically assessed the relation between the closure relation obeyed by generic LBM reflection-type rules and the target slip velocity boundary condition, explicitly formulating for the first time the main underlying assumptions. Second, we revisited previous LBM implementations of slip boundary schemes, with focus on the extension of the multireflection approach to handle the slip-flow regime [68]. Here, we discussed the accuracy of different classes of boundary schemes as slip boundary conditions. Moreover, the stability topic was also discussed, attempting to clarify possible sources of instability and presenting a general, but straightforward remedy to enhance the numerical stability range of parabolic slip velocity schemes. Third and final, we examined the quality of the different LBM families of slip boundary schemes, including comparisons with the well-established finite element method (FEM), by simulating two classical benchmark flow problems of slip over nonplanar solid surfaces, namely: (i) the cylindrical Couette flow [74–77] and (ii) the square array of circular cylinders traversed by a gaseous slow flow in the slip-flow regime [78–82]. The numerical results supported the theoretical conclusions, namely: *when equipped with slip boundary schemes of parabolic accuracy LBM is a competitive second-order accurate CFD tool to simulate slippage phenomena over arbitrarily nonplanar surfaces*. The linear slip schemes, while slightly degrading accuracy, are also appealing due to their improved stability characteristics and much simpler operating principle, using one node only. Overall, these conclusions establish the LBM as a very attractive CFD technique for simulating isothermal microfluidic flows in the slip-flow regime, a result that shall be further explored in future studies. In this respect, we believe that the present results can be further improved by removing the constant slip velocity constraint, e.g., by canceling the $\frac{\partial j_\theta}{\partial \theta}$ term directly with finite differences as suggested in [70] or possibly through more elegant approaches. In future studies we plan to investigate alternative ways to correct this issue directly at the level of the LBM populations, e.g., by reformulating the operation principe of LBM boundary schemes with respect to the way they handle normal and tangential components. For this task, a possible route may be exploring the ideas of Refs. [104,121] or [47,122–124], these latter originally proposed for Neumann- and Robin-type conditions in advection-diffusion problems. Also, for future work we plan to study the coupling of these slip boundary schemes with extended hydrodynamic models, where a Kn-based viscosity definition is incorporated in the NSE formulation to mimic the Knudsen layer near wall effects, e.g., Refs. [40,56,58,65]. Finally, to further consolidate the state-of-the-art on this subject, we emphasize the need for a critical assessment on the relative performance between the two modeling perspectives currently competing in the LBM simulation of the slip-flow regime, namely: the present approach based on standard lattices with high accuracy slip boundary schemes, e.g., Refs. [68–70] against those adopting the transcription of kinetic-theory-based boundary schemes over high-order LBM discretizations, based on high-order lattices, e.g., Refs. [60,125–128].

ACKNOWLEDGMENTS

The author is deeply thankful to Irina Ginzburg for the many discussions, clarifications, and suggestions provided during the carrying out of this work. Also, fruitful discussions with Prof. Viriato Semiao are acknowledged. The financial support given by Fundação para a Ciência e Tecnologia (FCT) through Grant No. SFRH/BPD/111228/2015 is also acknowledged.

APPENDIX A: DERIVATION OF THE PARABOLIC SLIP MULTIREFLECTION SCHEMES FOR THE SLIP VELOCITY BOUNDARY CONDITION

The purpose of this Appendix is to outline the main steps behind the derivation of multireflection schemes. Here, we revisit the procedure originally put forward in Refs. [46,47] and explain the derivation of the coefficients of the parabolic slip schemes, as presented in Table II.

1. Introductory material

Let us rewrite Eq. (21), the generic multireflection (MR) update rule [46,47], to implement in the LBM algorithm:

$$\begin{aligned} f_{\bar{q}}(\vec{x}_{\rm b}, t+1) = {} & \kappa_1\, \tilde{f}_q(\vec{x}_{\rm b}, t) + \kappa_0\, f_q(\vec{x}_{\rm b}, t+1) + \tilde{\kappa}_{-1}\, \tilde{f}_{\bar{q}}(\vec{x}_{\rm b}, t) \\ & + \kappa_{-1}\, f_q(\vec{x}_{\rm b} - \vec{c}_q, t+1) + \tilde{\kappa}_{-2}\, \tilde{f}_{\bar{q}}(\vec{x}_{\rm b} - \vec{c}_q, t) \\ & + F_q^{p.c.}(\vec{x}_{\rm b}, t) - \alpha^{(u)}\, j^{\star}_{q\,w}(\vec{x}_w, t). \end{aligned} \tag{A1}$$

Recall, $\vec{x}_{\rm b}$ is the boundary node and the wall located is at $\vec{x}_{\rm w} = \vec{x}_{\rm b} + \delta_q \vec{c}_q$. The goal is to find adequate values for the interpolation coefficients $\{\kappa_1, \kappa_0, \bar{\kappa}_{-1}, \kappa_{-1}, \bar{\kappa}_{-2}\}$, together with the correction parameters $F_q^{\rm p.c.}$ and $\alpha^{(u)}$, so that the slip closure relation, given by Eq. (12), is recovered, which we rewrite as follows:

$$\begin{aligned} & j_q(\vec{x}_b) + \alpha_q^+\, \partial_q j_q(\vec{x}_b) + \alpha_q^-\, \partial_q^2 j_q(\vec{x}_b) = j_{q\,w}(\vec{x}_{\rm w}), \\ & \alpha_q^+ := (\delta_q + \mathcal{C}\,\lambda_q), \quad \alpha_q^- := \left(\frac{\delta_q^2}{2} + \mathcal{C}\,\lambda_q\,\delta_q\right), \\ & \lambda_q := \frac{\lambda}{\Theta_q}, \quad \Theta_q := (\vec{c}_q \cdot \vec{n}), \quad \vec{x}_{\rm w} = \vec{x}_{\rm b} + \vec{c}_q\,\delta_q. \end{aligned} \tag{A2}$$

2. Preliminary manipulations

The analysis start by expressing the LBM populations at both post-stream and post-collision states in the more convenient form:

$$f_q = e_q^+ + e_q^- - \left(\Lambda^+ + \frac{1}{2}\right) g_q^+ - \left(\Lambda^- + \frac{1}{2}\right) g_q^-, \tag{A3a}$$

$$\tilde{f}_q = e_q^+ + e_q^- - \left(\Lambda^+ - \frac{1}{2}\right) g_q^+ - \left(\Lambda^- - \frac{1}{2}\right) g_q^-. \tag{A3b}$$

Recall, the post-collision components $g_q^{\pm}$ relate to the nonequilibrium $n_q^{\pm} = (f_q^{\pm} - e_q^{\pm})$ by $g_q^{\pm} = -s^{\pm}\, n_q^{\pm}$, where $e_q^{\pm}$ denotes the (symmetric/antisymmetric) equilibrium components and $s^{\pm}$ the (symmetric/antisymmetric) relaxation rates of the collision process. The associated relaxation eigenfunctions are defined as $\Lambda^{\pm} = (\frac{1}{s^{\pm}} - \frac{1}{2})$.

Based on the above preparations, we substitute Eqs. (A3) into Eq. (A2), and obtain

$$\begin{aligned} & \left[e_{\bar{q}}^+ + e_{\bar{q}}^- - \left(\Lambda^+ + \frac{1}{2}\right) g_{\bar{q}}^+ - \left(\Lambda^- + \frac{1}{2}\right) g_{\bar{q}}^-\right](\vec{x}_{\rm b}) \\ & = \kappa_1 \left[e_q^+ + e_q^- - \left(\Lambda^+ - \frac{1}{2}\right) g_q^+ - \left(\Lambda^- - \frac{1}{2}\right) g_q^-\right](\vec{x}_{\rm b}) + \kappa_0 \left[e_q^+ + e_q^- - \left(\Lambda^+ + \frac{1}{2}\right) g_q^+ - \left(\Lambda^- + \frac{1}{2}\right) g_q^-\right](\vec{x}_{\rm b}) \\ & \quad + \tilde{\kappa}_{-1} \left[e_{\bar{q}}^+ + e_{\bar{q}}^- - \left(\Lambda^+ - \frac{1}{2}\right) g_{\bar{q}}^+ - \left(\Lambda^- - \frac{1}{2}\right) g_{\bar{q}}^-\right](\vec{x}_{\rm b}) + \kappa_{-1} \left[e_q^+ + e_q^- - \left(\Lambda^+ + \frac{1}{2}\right) g_q^+ - \left(\Lambda^- + \frac{1}{2}\right) g_q^-\right](\vec{x}_{\rm b} - \vec{c}_q) \\ & \quad + \tilde{\kappa}_{-2} \left[e_{\bar{q}}^+ + e_{\bar{q}}^- - \left(\Lambda^+ - \frac{1}{2}\right) g_{\bar{q}}^+ - \left(\Lambda^- - \frac{1}{2}\right) g_{\bar{q}}^-\right](\vec{x}_{\rm b} - \vec{c}_q) + F_q^{p.c.}(\vec{x}_{\rm b}) - \alpha^{(u)}\, j^{\star}_{q\,w}(\vec{x}_{\rm w}). \end{aligned} \tag{A4}$$

As next step, we invoke the parity definitions, i.e., for any arbitrary ψ_q, we have $\psi_q^+ = \psi_{\bar{q}}^+$ and $\psi_q^- = -\psi_{\bar{q}}^-$, and group the coefficients in each term to simplify:

$$\begin{aligned} & \mathcal{A}^+\, e_q^+(\vec{x}_{\rm b}) + \mathcal{A}^-\, e_q^-(\vec{x}_{\rm b}) + \mathcal{B}^+\, g_q^+(\vec{x}_{\rm b}) + \mathcal{B}^-\, g_q^-(\vec{x}_{\rm b}) + \mathcal{C}^+\, e_q^+(\vec{x}_{\rm b} - \vec{c}_q) + \mathcal{C}^-\, e_q^-(\vec{x}_{\rm b} - \vec{c}_q) + \mathcal{D}^+\, g_q^+(\vec{x}_{\rm b} - \vec{c}_q) \\ & \quad + \mathcal{D}^-\, g_q^-(\vec{x}_{\rm b} - \vec{c}_q) + F_q^{\rm p.c.}(\vec{x}_{\rm b}) - \alpha^{(u)}\, j^{\star}_{q\,w}(\vec{x}_{\rm w}) = 0, \end{aligned} \tag{A5}$$

with

$$\begin{aligned} & \mathcal{A}^+ = \kappa_1 + \kappa_0 + \tilde{\kappa}_{-1} - 1, \quad \mathcal{A}^- = \kappa_1 + \kappa_0 - \tilde{\kappa}_{-1} + 1, \quad \mathcal{B}^+ = (\kappa_1 + \tilde{\kappa}_{-1}) - (\kappa_1 + \kappa_0 + \tilde{\kappa}_{-1} - 1)\left(\Lambda^+ + \frac{1}{2}\right), \\ & \mathcal{B}^- = (\kappa_1 - \tilde{\kappa}_{-1}) - (\kappa_1 + \kappa_0 - \tilde{\kappa}_{-1} + 1)\left(\Lambda^- + \frac{1}{2}\right), \quad \mathcal{C}^+ = (\kappa_{-1} + \tilde{\kappa}_{-2}), \quad \mathcal{C}^- = (\kappa_{-1} - \tilde{\kappa}_{-2}), \quad \mathcal{D}^+ = -\frac{1}{2}\,\mathcal{C}^- - \Lambda^+\,\mathcal{C}^+, \\ & \mathcal{D}^- = -\frac{1}{2}\,\mathcal{C}^+ - \Lambda^-\,\mathcal{C}^-. \end{aligned} \tag{A6}$$

3. Chapman-Enskog expansion approximation

At this point, we unfold the content of equilibrium and nonequilibrium populations. We recall the equilibrium was written in Eq. (3) and is given by

$$e_q^+ = t_q^{\star}\left(P + \frac{3\, j_q^2 - \|\vec{j}\|^2}{2\bar{\rho}}\right), \tag{A7a}$$

$$e_q^- = t_q^{\star}\,(j_q + \Lambda^-\, F_q), \tag{A7b}$$

where $j_q = \vec{c}_q \cdot \vec{j}$ and $F_q = \vec{c}_q \cdot \vec{F}$. As for the nonequilibrium post-collision quantities $g_q^{\pm}$, we can express them in approximated form, according to the second-order Chapman-Enskog expansion. We recall it was given in Eq. (7) as follows:

$$g_q^+ = \partial_q(e_q^- - \Lambda^- \partial_q e_q^+) \simeq t_q^\star \, \partial_q j_q, \tag{A8a}$$

$$g_q^- = \partial_q(e_q^+ - \Lambda^+ \partial_q e_q^-) \simeq t_q^\star \, \partial_q \left(P + \frac{3\, j_q^2 - \|\vec{j}\|^2}{2\bar{\rho}} \right) - \Lambda^+ t_q^\star \, \partial_q^2 j_q. \tag{A8b}$$

Note, Eqs. (A8) include a residue of $O(\epsilon^3)$, which we omit to alleviate notation. In consistency with the scaling of this order of approximation, we have neglected the second-order derivatives of pressure and nonlinear momentum terms (recall the derivation of the NSE, cf. Sec. II). Moreover, we have also assumed a constant body force.

4. Taylor expansion approximation

Next, we approximate the content of $e_q^{\pm}$ and $g_q^{\pm}$ from sites $\vec{x}_\mathrm{b} - \vec{c}_q$ to $\vec{x}_\mathrm{b}$. To execute this task, the content of these terms is approximated via the second-order Taylor expansion (again, using the fact that second-order derivatives of pressure and nonlinear momentum terms are negligible, according to the $O(\epsilon^3)$ scaling, and that the body force is constant):

$$e_q^+(\vec{x}_\mathrm{b} - \vec{c}_q) \simeq [e_q^+ - \partial_q e_q^+](\vec{x}_\mathrm{b}) \simeq t_q^\star \left[\left(P + \frac{3\, j_q^2 - \|\vec{j}\|^2}{2\bar{\rho}} \right) - \partial_q \left(P + \frac{3\, j_q^2 - \|\vec{j}\|^2}{2\bar{\rho}} \right) \right](\vec{x}_\mathrm{b}), \tag{A9a}$$

$$e_q^-(\vec{x}_\mathrm{b} - \vec{c}_q) \simeq \left[e_q^- - \partial_q e_q^- + \frac{1}{2}\, \partial_q^2 e_q^- \right](\vec{x}_\mathrm{b}) \simeq t_q^\star \left[j_q + \Lambda^- \, F_q - \partial_q j_q + \frac{1}{2}\, \partial_q^2 j_q \right](\vec{x}_\mathrm{b}), \tag{A9b}$$

$$g_q^+(\vec{x}_\mathrm{b} - \vec{c}_q) \simeq [g_q^+ - \partial_q g_q^+](\vec{x}_\mathrm{b}) \simeq t_q^\star \left[\partial_q j_q - \partial_q^2 j_q \right](\vec{x}_\mathrm{b}), \tag{A9c}$$

$$g_q^-(\vec{x}_\mathrm{b} - \vec{c}_q) \simeq g_q^-(\vec{x}_\mathrm{b}) \simeq t_q^\star \left[\partial_q \left(P + \frac{3\, j_q^2 - \|\vec{j}\|^2}{2\bar{\rho}} \right) - \Lambda^+ \, \partial_q^2 j_q \right](\vec{x}_\mathrm{b}). \tag{A9d}$$

5. Intermediate manipulations

At last, we substitute Eqs. (A7), (A8), and (A9) into Eq. (A5), and obtain

$$\begin{aligned} &\mathcal{A}^+ \left(P + \frac{3\, j_q^2 - \|\vec{j}\|^2}{2\bar{\rho}} \right) + \mathcal{A}^- \left(j_q + \Lambda^- \, F_q \right) + \mathcal{B}^+ \, \partial_q j_q + \mathcal{B}^- \left[\partial_q \left(P + \frac{3\, j_q^2 - \|\vec{j}\|^2}{2\bar{\rho}} \right) - \Lambda^+ \, \partial_q^2 j_q \right] \\ &+ \mathcal{C}^+ \left[\left(P + \frac{3\, j_q^2 - \|\vec{j}\|^2}{2\bar{\rho}} \right) - \partial_q \left(P + \frac{3\, j_q^2 - \|\vec{j}\|^2}{2\bar{\rho}} \right) \right] + \mathcal{C}^- \left(j_q + \Lambda^- \, F_q - \partial_q j_q + \frac{1}{2}\, \partial_q^2 j_q \right) \\ &+ \mathcal{D}^+ \left(\partial_q j_q - \partial_q^2 j_q \right) + \mathcal{D}^- \left[\partial_q \left(P + \frac{3\, j_q^2 - \|\vec{j}\|^2}{2\bar{\rho}} \right) - \Lambda^+ \, \partial_q^2 j_q \right] + \frac{1}{t_q^\star} \, F_q^{\mathrm{p.c.}} - \alpha^{(u)} \, j_{q\,w}(\vec{x}_\mathrm{w}) = 0. \end{aligned} \tag{A10}$$

Due to the Taylor expansion approximation, all terms in Eq. (A10), except $j_{q\,w}(\vec{x}_\mathrm{w})$, have been redefined over the $\vec{x}_\mathrm{b}$ location, and to alleviate notation we have dropped the dependency on $\vec{x}_\mathrm{b}$. The next step in the simplification routine takes into account that $\mathcal{D}^+ = -\frac{1}{2}\,\mathcal{C}^- - \Lambda^+ \mathcal{C}^+$ and $\mathcal{D}^- = -\frac{1}{2}\,\mathcal{C}^+ - \Lambda^- \mathcal{C}^-$. Then, we collect the coefficients of identical terms as follows:

$$\begin{aligned} &(\mathcal{A}^+ + \mathcal{C}^+) \left(P + \frac{3\, j_q^2 - \|\vec{j}\|^2}{2\bar{\rho}} \right) + (\mathcal{A}^- + \mathcal{C}^-) \left(j_q + \Lambda^- \, F_q \right) + \left(\mathcal{B}^+ - \frac{3}{2}\, \mathcal{C}^- - \Lambda^+ \mathcal{C}^+ \right) \partial_q j_q + \left(\mathcal{B}^- - \frac{3}{2}\, \mathcal{C}^+ - \Lambda^- \mathcal{C}^- \right) \\ &\times \partial_q \left(P + \frac{3\, j_q^2 - \|\vec{j}\|^2}{2\bar{\rho}} \right) + \left(-\Lambda^+ \mathcal{B}^- + \frac{3}{2}\, \Lambda^+ \mathcal{C}^+ + (1 + \Lambda) \mathcal{C}^- \right) \partial_q^2 j_q + \frac{1}{t_q^\star} \, F_q^{p.c.} - \alpha^{(u)} \, j_{q\,w}(\vec{x}_\mathrm{w}) = 0. \end{aligned} \tag{A11}$$

At last, we re-express Eq. (A12) in a more convenient form, i.e., similar to Eq. (A2):

$$\begin{aligned} &(\mathcal{A}^- + \mathcal{C}^-) \, j_q + \left(\mathcal{B}^+ - \frac{3}{2}\, \mathcal{C}^- - \Lambda^+ \mathcal{C}^+ \right) \partial_q j_q + \mathcal{C}^- \, \partial_q^2 j_q - \alpha^{(u)} \, j_{q\,w}(\vec{x}_\mathrm{w}) + (\mathcal{A}^+ + \mathcal{C}^+) \left(P + \frac{3\, j_q^2 - \|\vec{j}\|^2}{2\bar{\rho}} \right) \\ &- \Lambda^- (\mathcal{A}^- + \mathcal{C}^-) \, F_q + \left(\mathcal{B}^- - \frac{3}{2}\, \mathcal{C}^+ - \Lambda^- \mathcal{C}^- \right) \left[\partial_q \left(P + \frac{3\, j_q^2 - \|\vec{j}\|^2}{2\bar{\rho}} \right) - \Lambda^+ \, \partial_q^2 j_q \right] + \frac{1}{t_q^\star} \, F_q^{\mathrm{p.c.}} = 0. \end{aligned} \tag{A12}$$

6. Final manipulations

The final step consists of determining the five interpolation coefficients $\{\kappa_1, \kappa_0, \bar{\kappa}_{-1}, \kappa_{-1}, \bar{\kappa}_{-2}\}$ present in the $\{\mathcal{A}^{\pm}, \mathcal{B}^{\pm}, \mathcal{C}^{\pm}\}$ terms, as given by Eq. (A6), plus the correction $F_q^{\text{p.c.}}$ as function of $\alpha^{(u)}$ to recover the target closure relation given by Eq. (A2). This procedure leads to the following six conditions:

(1) The coefficient in j_q must be: $(\mathcal{A}^- + \mathcal{C}^-) = \alpha^{(u)}$.

(2) The coefficient in $\partial_q j_q$ must be: $(\mathcal{B}^+ - \frac{3}{2}\mathcal{C}^- - \Lambda^+ \mathcal{C}^+) = \alpha^{(u)}\,\alpha_q^+$

(3) The coefficient in $\partial_q^2 j_q$ term must be: $\mathcal{C}^- = \alpha^{(u)}\,\alpha_q^-$.

(4) The coefficient in $(P + \frac{3\,j_q^2 - \|\vec{j}\|^2}{2\bar{\rho}})$ must nullify this term, that is: $(\mathcal{A}^+ + \mathcal{C}^+) = 0$.

(5) The coefficient in $[\partial_q (P + \frac{3\,j_q^2 - \|\vec{j}\|^2}{2\bar{\rho}}) - \Lambda^+\,\partial_q^2 j_q]$ must equal that of F_q, that is $(\mathcal{B}^- - \frac{3}{2}\,\mathcal{C}^+ - \Lambda^-\,\mathcal{C}^-) = -\Lambda^-(\mathcal{A}^- + \mathcal{C}^-) = -\alpha^{(u)}\,\Lambda^-$.

(6) The post-collision correction $F_q^{p.c.}$ is used to cancel out the last two terms, which recalling Eq. (A8b) and $F_q^\star = t_q^\star\,F_q$, leads to $F_q^{\text{p.c.}} = \alpha^{(u)}\,\Lambda^-(g_q^- - F_q^\star)$.

The system is now closed, and solutions are parametrized by $\alpha^{(u)}$ [46,47]. A general methodology, called MR(k_q) family [46], proposes to reparametrize the solutions in terms of a free parameter k_q. Following stability and accuracy arguments, the original works [46,47] suggested to take $\alpha^{(u)} = \frac{2}{1+k_q}$. Based on this reparametrization, and after some simple algebraic manipulations, the simultaneous solution of conditions from (1) to (5) leads to the coefficients displayed in Table II. Then, the particular choice of the k_q parameter may produce different multireflection subfamilies, such as $k_q = (-\frac{1}{2} + \alpha_q^+ + \alpha_q^-)$ for MR1 and $k_q = (-\frac{1}{2} + \alpha_q^+ + \alpha_q^- - C\,\Lambda^-)$ for MGMR(C), as pointed out in Sec. IV and detailed in Ref. [47].

To conclude, we reiterate that the procedure here summarized corresponds to that developed in Refs. [46,47] for the no-slip case. In fact, the original no-slip results [46,47] are contained in our slip formulas by vanishing the slippage contribution. Another way to view the similitude between the slip and the no-slip multireflection formulas is that one can be reduced to another through the transformations: $\alpha_q^+ \to \delta_q$ and $\alpha_q^- \to \frac{\delta_q^2}{2}$. Explicitly, the slip coefficients shown in Table II reduce to the no-slip coefficients shown in Table II of Ref. [46] or in Table 2 of Ref. [47]. For the LBM users the major interest behind this similitude lies in the possibility of reusing pre-existing LBM codes already installed with no-slip multireflection schemes [46,47] to model slip-flows. By simply re-expressing the multireflection coefficients from no-slip to slip ones the slip boundary conditions here derived can be made available, while the rest of the numerical algorithm remains unchanged.

APPENDIX B: POSSIBLE ALTERNATIVE FOR REFERENCE SOLUTION IN SECTION VII

The determination of the effective permeability k_{eff} of a slow flow past a periodic array of cylinders has been tackled through a number of mathematical techniques, which go from elliptic functions in Ref. [129], to the collocation of harmonics in Ref. [130], or the use of distributed singularities in Ref. [131]. Yet, most of these works have only been concerned with the case of no-slip boundaries. To the best of our knowledge, the extension of these techniques to the slip-flow regime has not been reported, and the only results available have been obtained with the cell model [118–120].

The cell model formulates in the low solid fraction limit, whereby the system may be reduced to one representative cell that encloses one solid obstacle. The effects of the neighboring cells are exclusively accounted for on the cell outer boundary condition. This last step is the key element of the method: despite the considerably simplification over the underlying analytical approach, it inevitably introduces some level of approximation. Here, we follow Ref. [132], which proposed extending the original Kuwabara cell model [118] to include the slip boundary condition, Eq. (1). This procedure leads to the following k_{eff} solution:

$$k_{\text{eff}} = \frac{1}{16\,p^2\,(1+2\,\mathcal{C}\,\lambda)}\Bigg[4\,(1+2\,\mathcal{C}\,\lambda)\,\ln\left(\frac{1}{p}\right) - 3 - 2\,\mathcal{C}\,\lambda + 4\,p^2 - (1-2\,\mathcal{C}\,\lambda)p^4\Bigg]. \tag{B1}$$

In the continuum limit $\lambda \to 0$, Eq. (B1) reduces to the original Kuwabara cell model solution [118] for no-slip cylinders:

$$k_{\text{eff}} = \frac{1}{16\,p^2}\left[4\,\ln\left(\frac{1}{p}\right) - 3 + 4\,p^2 - p^4\right], \tag{B2}$$

which establishes the self-consistency of the slip-flow solution, Eq. (B1).

Although the cell model consists of an interesting theoretical tool, whether it yields sufficiently accurate solutions for the purpose of code verification does require a more in depth analysis. Given the lack of other reference solutions in the slip-flow regime, next we critically discuss the no-slip hydrodynamic regime, where rather accurate k_{eff} solutions are available [129–131,133]. To this end, let us take as reference the k_{eff} quasianalytical solution obtained with the modified multipole procedure reported in Refs. [46,133]. By comparing k_{eff} in Refs. [46,133] against k_{eff} predicted with the cell model, Eq. (B2), we observe a relative difference of $\approx$0.33% at $p = 0.2$, which is a rather acceptable error. However, repeating this comparison now between k_{eff} in Refs. [46,133] and FEM simulations run on a rather coarse mesh (e.g., with 50 computational cells along H and a discretization with quadratic elements) we obtain a relative difference of $\approx$0.008% at $p = 0.2$. That is, a relatively coarse FEM simulation manages to be about two orders of magnitude more accurate than cell model predictions (the same conclusion holds for LBM with parabolic schemes used as reference solver). For that reason, rather than using Eq. (B1) as k_{eff} reference solution, e.g., Refs. [71,81,85], we prefer adopting FEM simulations[1] run on finer meshes with higher-order elements as a means to establish the reference solution $k_{\text{eff}}^{(\text{ref})}$ to be used in Sec. VII; numerical details about those FEM simulations are given in Sec. VII A.

[1]The same task could have been done with LBM. Yet, we find FEM more appropriate for this task due to its role in this work. That is, FEM is taken as a well-established and well-validated numerical solver, whose solutions can be considered reference.

[1] C. Cercignani, *The Boltzmann Equation and Its Application* (Springer-Verlag, New York, 1988).

[2] I. N. Ivchenko, S. K. Loyalka, and Jr. R. V. Tompson, *Analytical Methods for Problems of Molecular Transport* (Springer, Berlin, 2007).

[3] M. N. Kogan, *Rarefied Gas Dynamics* (Plenum Press, New York, 1969).

[4] G. E. Uhlenbeck and G. W. Ford, *Lectures in Statistical Mechanics* (American Mathematical Society, Providence, RI, 1963).

[5] M. Gad-el-Hak, The fluid mechanics of microdevices: The freeman scholar lecture, ASME, J. Fluids Eng. **121**, 5 (1999).

[6] G. E. Karniadakis and A. Beskok, *Micro Flow: Fundamentals and Simulation* (Springer-Verlag, New York, 2001).

[7] P. Abgrall and N.-T. Nguyen, *Nanofluidics* (Artech House, Boston, 2009).

[8] F. Sharipov, Data on the velocity slip and temperature jump on a gas-solid interface, J. Phys. Chem. Ref. Data **40**, 023101 (2011).

[9] W.-M. Zhang, G. Meng, and X. Wei, A review on slip models for gas microflows, Microfluid Nanofluid **13**, 845 (2012).

[10] C.-M. Ho and Y.-C. Tai, Micro-electro-mechanical systems (MEMS) and fluid flows, Annu. Rev. Fluid Mech. **30**, 579 (1988).

[11] H. A. Stone, A. D. Stroock, and A. Ajdari, Engineering flows in small devices: Microfluidics toward a laboratory-on-a-chip, Annu. Rev. Fluid Mech. **36**, 381 (2004).

[12] F. Sharipov and V. Seleznev, Data on internal rarefied gas flows, J. Phys. Chem. Ref. Data **27**, 657 (1998).

[13] Y. Sone, *Kinetic Theory and Fluid Dynamics* (Birkhäuser, Boston, 2002).

[14] N. G. Hadjiconstantinou, The limits of Navier-Stokes theory and kinetic extensions for describing small-scale gaseous hydrodynamics, Phys. Fluids **18**, 111301 (2006).

[15] Y. Sone, *Molecular Gas Dynamics: Theory, Techniques, and Applications* (Birkhäuser, Boston, 2007).

[16] F. Coron, Derivation of slip boundary-conditions for the Navier-stokes system from the Boltzmann equation, J. Stat. Phys. **54**, 829 (1989).

[17] K. Aoki, S. Takata, and T. Nakanishi, Poiseuille-flow of a rarefied gas between two parallel plates driven by a uniform external force, Phys. Rev. E **65**, 026315 (2002).

[18] K. Aoki, H. Yoshida, T. Nakanishi, and A. L. Garcia, Inverted velocity profile in the cylindrical Couette flow of a rarefied gas, Phys. Rev. E **68**, 016302 (2003).

[19] J. Nassios and J. E. Sader, Asymptotic analysis of the Boltzmann-BGK equation for oscillatory flows, J. Fluid Mech. **708**, 197 (2012).

[20] S. Takata and M. Hattori, Asymptotic theory for the time-dependent behavior of a slightly rarefied gas over a smooth solid boundary, J. Stat. Phys. **147**, 1182 (2012).

[21] K. Aoki, S. Kosuge, T. Fujiwara, and T. Goudon, Unsteady motion of a slightly rarefied gas caused by a plate oscillating in its normal direction, Phys. Rev. Fluids **2**, 013402 (2017).

[22] K. Aoki, C. Baranger, M. Hattori, S. Kosuge, G. Martalo, J. Mathiaud, and L. Mieussens, Slip boundary conditions for the compressible Navier-Stokes equations, J. Stat. Phys. **169**, 744 (2017).

[23] J. C. Maxwell, On stresses in rarefied gases arising from inequalities of temperature, Philos. Trans. R. Soc. London **170**, 231 (1879).

[24] C. S. Wang-Chang and G. E. Uhlenbeck, Transport phenomena in very dilute gases, (Technical Report VMH-3-F, University of Michigan, 1949).

[25] E. P. Gross and S. Ziering, Boundary value problems in kinetic theory of gases, Ann. Phys. **1**, 141 (1957).

[26] S. K. Loyalka and R. V. Thompson, The velocity slip problem: Accurate solutions of BGK model integral equation, Euro. J. Mech. B/Fluids **28**, 211 (2009).

[27] J. Maurer, P. Tabeling, P. Joseph, and H. Willaime, Second-order slip laws in microchannels for helium and nitrogen, Phys. Fluids **15**, 2613 (2003).

[28] P. Taheri, A. S. Rana, M. Torrilhon, and H. Struchtrup, Macroscopic description of steady and unsteady rarefaction effects in boundary value problems of gas dynamics, Continuum Mech. Thermodyn. **21**, 423 (2009).

[29] X.-J. Gu, D. R. Emerson, and G.-H. Tang, Analysis of the slip coefficient and defect velocity in the Knudsen layer of a rarefied gas using linearized moment equations, Phys. Rev. E **81**, 016313 (2010).

[30] J. B. Young, Calculation of Knudsen layers and jump conditions using the linearised G13 and R13 moment methods, Int. J. Heat Mass Transf. **54**, 2902 (2011).

[31] C. Cercignani, P. Foresti, and F. Sernagiotto, Dependence of the slip coefficient on the form of the collision frequency, Nuovo Cimento B (1965-1970) **57**, 297 (1968).

[32] C. Cercignani, *Mathematical Methods in Kinetic Theory* (Plenum, New York, 1990).

[33] D. R. Willis, Comparison of kinetic theory analyses of linearized Couette flow, Phys. Fluids **5**, 127 (1962).

[34] S. K. Loyalka, N. Petrellis, and T. S. Storvick, Some numerical results for the BGK model: Thermal creep and viscous slip problems with arbitrary accommodation at the surface, Phys. Fluids **18**, 1094 (1975).

[35] S. K. Loyalka, The Qn and Fn integrals for the BGK model, Transp. Theory Stat. Phys. **4**, 55 (1975).

[36] R. Verfürth, Finite element approximation of incompressible Navier-Stokes equations with slip boundary condition, Numerische Mathematik **50**, 697 (1987).

[37] A. Liakos, Discretization of the Navier-Stokes equations with slip boundary condition, Numer. Methods Partial Dif. Equat. **17**, 26 (2001).

[38] S. Chen and G. D. Doolen, Lattice Boltzmann method for fluid flows, Annu. Rev. Fluid Mech. **30**, 329 (1998).

[39] S. Succi, *The Lattice Boltzmann Equation for Fluid Dynamics and Beyond* (Oxford University Press, Oxford, 2001).

[40] C. K. Aidun and J. R. Clausen, Lattice-Boltzmann method for complex flows, Annu. Rev. Fluid Mech. **42**, 439 (2010).

[41] T. Krüger, H. Kusumaatmaja, A. Kuzmin, O. Shardt, G. Silva, and E. M. Viggen, *The Lattice Boltzmann Method—Principles and Practice* (Springer, Berlin, 2016).

[42] O. Filippova and D. Hanel, Grid refinement for lattice-BGK models, J. Comput. Phys. **147**, 219 (1998).

[43] M. Bouzidi, M. Firdaouss, and P. Lallemand, Momentum transfer of a Boltzmann-lattice fluid with boundaries, Phys. Fluids **13**, 3452 (2001).

[44] P. Lallemand and L.-S. Luo, Lattice Boltzmann method for moving boundaries, J. Comput. Phys. **184**, 406 (2003).

[45] D. Yu, R. Mei, L.-S. Luo, and W. Shyy, Viscous flow computations with the method of lattice Boltzmann equation, Prog. Aerosp. Sci. **39**, 329 (2003).
[46] I. Ginzburg and D. d'Humières, Multireflection boundary conditions for lattice Boltzmann models, Phys. Rev. E **68**, 066614 (2003).
[47] I. Ginzburg, F. Verhaeghe, and D. d'Humières, Two-relaxation-times lattice Boltzmann scheme: About parametrization, velocity, pressure and mixed boundary conditions, Commun. Comput. Phys. **3**, 427 (2008).
[48] S. Khirevich, I. Ginzburg, and U. Tallarek, Coarse- and fine-grid numerical behavior of MRT/TRT lattice-Boltzmann schemes in regular and random sphere packings, J. Comput. Phys. **281**, 708 (2015).
[49] S. Ansumali and I. V. Karlin, Kinetic boundary conditions in the lattice Boltzmann method, Phys. Rev. E **66**, 026311 (2002).
[50] C. Y. Lim, C. Shu, X. D. Niu, and Y. T. Chew, Application of lattice Boltzmann method to simulate microchannel flows, Phys. Fluids **14**, 2299 (2002).
[51] X. Nie, G. D. Doolen, and S. Chen, Lattice-Boltzmann simulations of fluid flows in MEMS, J. Stat. Phys. **107**, 279 (2002).
[52] B. Li and D. Kwok, Discrete Boltzmann Equation for Microfluidics, Phys. Rev. Lett. **90**, 124502 (2003).
[53] T. Lee and C. L. Lin, Rarefaction and compressibility of the lattice Boltzmann equation method in a gas microchannel, Phys. Rev. E **71**, 046706 (2005).
[54] M. Sbragaglia and S. Succi, Analytical calculation of slip flow in lattice Boltzmann models with kinetic boundary conditions, Phys. Fluids **17**, 093602 (2005).
[55] Z. Chai, Z. Guo, L. Zheng, and B. Shi, Lattice Boltzmann simulation of surface roughness effect on gaseous flow in microchannel, J. Appl. Phys. **104**, 014902 (2008).
[56] S. H. Kim, H. Pitsch, and I. D. Boyd, Slip velocity and Knudsen layer in lattice Boltzmann method for microscale flows, Phys. Rev. E **77**, 026704 (2008).
[57] W. H. Yudistiawan, S. Ansumali, and I. V. Karlin, Hydrodynamics beyond Navier-Stokes: The slip flow model, Phys. Rev. E **78**, 016705 (2008).
[58] J. Zhang, Lattice Boltzmann method for microfluidics: Models and applications, Microfluid Nanofluid **10**, 1 (2010).
[59] N. Prasianakis and S. Ansumali, Microflow simulation via the lattice Boltzmann method, Commun. Comput. Phys. **9**, 1128 (2011).
[60] C. Feuchter and W. Schleifenbaum, High-order lattice Boltzmann models for wall-bounded flows at finite Knudsen numbers, Phys. Rev. E **94**, 013304 (2016).
[61] L.-S. Luo, Comment on "Discrete Boltzmann Equation for Microfluidics," Phys. Rev. Lett. **92**, 139401 (2004).
[62] Z. Guo, B. Shi, T. S. Zhao, and C. Zheng, Discrete effects on boundary conditions for the lattice Boltzmann equation in simulating microscale gas flows, Phys. Rev. E **76**, 056704 (2007).
[63] L.-S. Luo, Comment on "Heat transfer and fluid flow in microchannels and nanochannels at high Knudsen number using thermal lattice-Boltzmann method," Phys. Rev. E **84**, 048301 (2011).
[64] K. Suga, Lattice Boltzmann method for complex micro-flows: Applicability and limitations for practical applications, Fluid Dyn. Res. **45**, 034501 (2013).
[65] Z. Guo and C. Zheng, Analysis of lattice Boltzmann equation for microscale gas flows: Relaxation time, Boundary condition, and Knudsen layer, Int. J. Comput. Fluid Dyn. **22**, 465 (2008).
[66] F. Verhaeghe, L.-S. Luo, and B. Blanpain, Lattice Boltzmann modeling of microchannel flow in slip flow regime, J. Comput. Phys. **228**, 147 (2009).
[67] S. Tao and Z. Guo, Boundary condition for lattice Boltzmann modeling of microscale gas flows with curved walls in the slip regime, Phys. Rev. E **91**, 043305 (2015).
[68] G. Silva and V. Semiao, Consistent lattice Boltzmann modeling of low-speed isothermal flows at finite Knudsen numbers in slip-flow regime: Application to plane boundaries, Phys. Rev. E **96**, 013311 (2017).
[69] S. Izquierdo and N. Fueyo, Momentum transfer correction for macroscopic-gradient boundary conditions in lattice Boltzmann methods, J. Comput. Physics **229**, 2497 (2010).
[70] T. Reis and P. J. Dellar, Lattice Boltzmann simulations of pressure-driven flows in microchannels using Navier-Maxwell slip boundary conditions, Phys. Fluids **24**, 112001 (2012).
[71] L. Wang and X. Yin, Apparent permeability of flow through periodic arrays of spheres with first-order slip, Powder Technol. **311**, 313 (2017).
[72] A. Pasquali, M. Geier, and M. Krafczyk, Near-wall treatment for the simulation of turbulent flow by the cumulant lattice Boltzmann method, Comput. Math. Appl. (2017), doi:10.1016/j.camwa.2017.11.022.
[73] Comsol, *COMSOL Multiphysics User's Guide 5.0*, July edition (2015).
[74] D. Einzel, P. Panzer, and M. Liu, Boundary Condition for Fluid Flow: Curved or Rough Surfaces, Phys. Rev. Lett. **64**, 2269 (1990).
[75] K. W. Tibbs, F. Baras, and A. L. Garcia, Anomalous flow profile due to the curvature effect on slip length, Phys. Rev. E **56**, 2282 (1997).
[76] S. Yuhong, R. W. Barber, and D. R. Emerson, Inverted velocity profiles in rarefied cylindrical Couette gas flow and the impact of the accommodation coefficient, Phys. Fluids **17**, 047102 (2005).
[77] D. A. Lockerby, J. M. Reese, D. R. Emerson, and R. W. Barber, Velocity boundary condition at solid walls in rarefied gas calculations, Phys. Rev. E **70**, 017303 (2004).
[78] J. Wang, L. Chen, Q. Kang, and S. S. Rahman, The lattice Boltzmann method for isothermal micro-gaseous flow and its application in shale gas flow: A review, Int. J. Heat Mass Transf. **95**, 94 (2016).
[79] B. Zhou, P. J. Jiang, R. Xu, and X. Ouyang, General slip regime permeability model for gas flow through porous media, Phys. Fluids **28**, 072003 (2016).
[80] J. Zhao, J. Yao, A. Li, M. Zhang, L. Zhang, Y. Yang, and H. Sun, Simulation of microscale gas flow in heterogeneous porous media based on the lattice Boltzmann method, J. Appl. Phys. **120**, 084306 (2016).
[81] L. Wu, M. T. Ho, L. Germanou, X.-J. Gu, C. Liu, K. Xu, and Y. Zhang, On the apparent permeability of porous media in rarefied gas flows, J. Fluid Mech. **822**, 398 (2017).
[82] S. Singh, F. Jiang, and T. Tsuji, Impact of the kinetic boundary condition on porous media flow in the lattice Boltzmann formulation, Phys. Rev. E **96**, 013303 (2017).

[83] Z. Guo, B. Shi, and C. Zheng, Velocity inversion of micro cylindrical Couette flow: A lattice Boltzmann study, Comput. Math. Appl. **61**, 3519 (2011).
[84] M. Watari, Rotational slip flow in coaxial cylinders by the finite-difference lattice boltzmann methods, Comput. Phys. **9**, 1293 (2011).
[85] Z. Chai, B. Shi, Z. Guo, and J. Lu, Gas flow through square arrays of circular cylinders with Klinkenberg effect: A lattice Boltzmann study, Commun. Comput. Phys. **8**, 1052 (2010).
[86] R. Arabjamaloei and D. W. Ruth, Lattice Boltzmann based simulation of gas flow regimes in low permeability porous media: Klinkenberg's region and beyond, J. Nat. Gas. Sci. Eng. **31**, 405 (2016).
[87] S. Tao, H. Zhang, and Z. Guo, Drag correlation for micro spherical particles at finite Reynolds and Knudsen numbers by lattice Boltzmann simulations, J. Aerosol. Sci. **103**, 105 (2017).
[88] I. Ginzburg, F. Verhaeghe, and D. d'Humières, Study of simple hydrodynamic solutions with the two-relaxation-times lattice Boltzmann scheme, Commun. Comput. Phys. **3**, 519 (2008).
[89] I. Ginzburg, Consistent lattice Boltzmann schemes for the Brinkman model of porous flow and infinite Chapman-Enskog expansion, Phys. Rev. E **77**, 066704 (2008).
[90] D. d'Humières and I. Ginzburg, Viscosity independent numerical errors for Lattice Boltzmann models: From recurrence equations to "magic" collision numbers, Comput. Math. Appl. **58**, 823 (2009).
[91] I. Ginzburg, Truncation errors, exact and heuristic stability analysis of two-relaxation-times lattice boltzmann schemes for anisotropic advection-diffusion equation, Commun. Comput. Phys. **11**, 1439 (2012).
[92] L. Talon, D. Bauer, N. Gland, S. Youssef, H. Auradou, and I. Ginzburg, Assessment of the two relaxation time Lattice-Boltzmann scheme to simulate Stokes flow in porous media, Water Resour. Res. **48**, W04526 (2012).
[93] Y. H. Qian, D. d'Humiéres, and P. Lallemand, Lattice BGK models for Navier-Stokes equation, Europhys. Lett. **17**, 479 (1992).
[94] I. Ginzburg, D. d'Humières, and A. Kuzmin, Optimal stability of advection-diffusion lattice Boltzmann models with two relaxation times for positive/negative equilibrium, J. Stat. Phys. **139**, 1090 (2010).
[95] U. Frisch, D. d'Humières, B. Hasslacher, P. Lallemand, Y. Pomeau, and J.-P. Rivet, Lattice-gas hydrodynamics in two and three dimensions, Complex Syst. **1**, 649 (1987).
[96] X. He and L.-S. Luo, Lattice Boltzmann model for the incompressible Navier-Stokes equation, J. Stat. Phys. **88**, 927 (1997).
[97] J. M. Buick and C. A. Greated, Gravity in a lattice Boltzmann model, Phys. Rev. E **61**, 5307 (2000).
[98] G. Silva and V. Semiao, A study on the inclusion of body forces in the lattice Boltzmann BGK equation to recover steady-state hydrodynamics, Physica A **390**, 1085 (2011).
[99] G. Silva and V. Semiao, First- and second-order forcing expansions in a lattice Boltzmann method reproducing isothermal hydrodynamics in artificial compressibility form, J. Fluid Mech. **698**, 282 (2012).
[100] S. Chapman and T. G. Cowling, *The Mathematical Theory of Non-uniform Gases* (Cambridge University Press, Cambridge, 1952).
[101] R. Cornubert, D. d'Humiéres, and D. Levermore, A Knudsen layer theory for lattice Gases, Physica D **47**, 241 (1991).
[102] I. Ginzbourg and P. M. Adler, Boundary flow condition analysis for the three-dimensional lattice Boltzmann model, J. Phys. II **4**, 191 (1994).
[103] L. Szalmas, Slip-flow boundary condition for straight walls in the lattice Boltzmann model, Phys. Rev. E **73**, 066710 (2006).
[104] I. Ginzbourg and D. d'Humières, Local second-order boundary methods for lattice Boltzmann models, J. Stat. Phys. **84**, 927 (1996).
[105] J. Trapp and J. D. Ramshaw, A simple heuristic method for analyzing the effect of boundary conditions on numerical stability, J. Comput. Physics **20**, 238 (1975).
[106] J. H. Ferziger and M. Peric, *Computational Methods for Fluid Dynamics*, 3rd ed. (Springer, Berlin, 2002).
[107] C. A. J. Fletcher, *Computational Techniques for Fluid Dynamics*, Vol. 1: Fundamental and General Techniques, 2nd ed. (Springer-Verlag, Berlin, 1991).
[108] M. Junk and Z. Yang, Convergence of lattice Boltzmann methods for Stokes flows in periodic and bounded domains, Comput. Math. Appl. **55**, 1481 (2008).
[109] P. Lallemand and L.-S. Luo, Theory of the lattice Boltzmann method: Dispersion, dissipation, isotropy, galilean invariance, and stability, Phys. Rev. E **61**, 6546 (2000).
[110] S. Tao, J. Hu, and Z. Guo, An investigation on momentum exchange methods and refilling algorithms for lattice Boltzmann simulation of particulate flows, Comput. Fluids **133**, 1 (2016).
[111] F. Gendre, D. Ricot, G. Fritz, and P. Sagaut, Grid refinement for aeroacoustics in the lattice Boltzmann method: A directional splitting approach, Phys. Rev. E **96**, 023311 (2017).
[112] X. Li, F. Jiang, and C. Hu, Analysis of the accuracy and pressure oscillations of the lattice Boltzmann method for fluid-solid interactions, Comput. Fluids **129**, 33 (2016).
[113] A. Dinler, R. W. Barber, D. R. Emerson, S. K. Stefanov, and K. Orucoglu, On the degree of boundary slip over nonplanar surfaces, Microfluid Nanofluid **15**, 807 (2013).
[114] J. N. Reddy, *An Introduction to the Finite Element Method* (McGraw-Hill, NY, 1993).
[115] I. Ginzburg, G. Silva, and L. Talon, Analysis and improvement of Brinkman lattice Boltzmann schemes: Bulk, boundary, interface. Similarity and distinctness with finite elements in heterogeneous porous media, Phys. Rev. E **91**, 023307 (2015).
[116] G. Silva, L. Talon, and I. Ginzburg, Low- and high-order accurate boundary conditions: From Stokes to Darcy porous flow modeled with standard and improved Brinkman lattice Boltzmann schemes, J. Comput. Phys. **335**, 50 (2017).
[117] G. Silva and I. Ginzburg, The permeability and quality of velocity field in a square array of solid and permeable cylindrical obstacles with the TRT-LBM and FEM Brinkman schemes, C. R. Mec. **343**, 545 (2015).
[118] S. Kuwabara, The forces experienced by randomly distributed parallel circular cylinders or spheres in a viscous flow at small Reynolds numbers, J. Phys. Soc. Jpn. **14**, 527 (1959).
[119] J. Happel and H. Brenner, *Low Reynolds Number Hydrodynamics* (Martinus Nijoff, The Hague, 1983).
[120] M. Maleki, R. J. Martinuzzi, W. Herzog, and S. Federico, Orthotropic hydraulic permeability of arrays of parallel cylinders, Phys. Rev. E **96**, 033112 (2017).

[121] I. Ginzburg and K. Steiner, Lattice Boltzmann model for free-surface flow and its application to filling process in casting, J. Comput. Phys. **185**, 61 (2003).

[122] I. Ginzburg, Generic boundary conditions for lattice Boltzmann models and their application to advection and anisotropic dispersion equations, Adv. Water Resour. **28**, 1196 (2005).

[123] L. Li, R. Mei, and J. F. Klausner, Boundary conditions for thermal lattice Boltzmann equation method, J. Comput. Phys. **237**, 366 (2013).

[124] T. Gebäck and A. Heintz, A lattice Boltzmann method for the advection-diffusion equation with Neumann boundary conditions, Commun. Comput. Phys. **15**, 487 (2014).

[125] V. E. Ambrus and V. Sofonea, Implementation of diffuse-reflection boundary conditions using lattice Boltzmann models based on half-space Gauss-Laguerre quadratures, Phys. Rev. E **89**, 041301(R) (2014).

[126] J. Meng and Y. Zhang, Diffuse reflection boundary condition for high-order lattice Boltzmann models with streaming-collision mechanism, J. Comput. Phys. **258**, 601 (2014).

[127] Y. Shi, Y. W. Yap, and J. E. Sader, Linearized lattice Boltzmann method for micro- and nanoscale flow and heat transfer, Phys. Rev. E **92**, 013307 (2015).

[128] A. Montessori, P. Prestininzi, M. La Rocca, and S. Succi, Lattice Boltzmann approach for complex nonequilibrium flows, Phys. Rev. E **92**, 043308 (2015).

[129] H. Hasimoto, On the periodic fundamental solutions of the Stokes equations and their application to viscous flow past a cubic array of spheres, J. Fluid Mech. **5**, 317 (1959).

[130] A. S. Sangani and A. Acrivos, Slow flow past periodic arrays of cylinders with application to heat transfer, Int. J. Multiph. Flow **8**, 193 (1982).

[131] J. E. Drummond and M. Tahir, Laminar viscous flow through regular arrays of parallel solid cylinders, Int. J. Multiph. Flow **10**, 515 (1987).

[132] Z. Chai, J. Lu, B. Shi, and Z. Guo, Gas slippage effect on the permeability of circular cylinders in a square array, Int. J. Heat Mass Transfer **54**, 3009 (2011).

[133] P. Adler, *Porous Media: Geometry and Transports* (Butterworth-Heinemann, Stoneham, MA, 1992).